Broadband Monolithic Constrained Lens Design

by

Leonard Thomas Hall

B.E. (Electrical & Electronic, with Honours),
The University of Adelaide, Australia, 2000

Thesis submitted for the degree of

Doctor of Philosophy

in

School of Electrical and Electronic Engineering,
Faculty of Engineering, Computer and Mathematical Sciences
The University of Adelaide, Australia

August, 2009

Chapter 3

Transmission Line & Network Theory

THE previous chapter describes a constrained lens as a number of antenna arrays and antenna elements, referred to as ports, connected in series by transmission lines. Efficient power transfer through a beamformer, and an array of antenna elements, is achieved by minimising the reflected power at every junction within the system. This is achieved by impedance matching each port, antenna element, and interconnecting transmission line to the impedance of the network at the connection point. This requires a detailed knowledge of microwave transmission line theory.

This chapter describes the principles of transmission line theory in detail. The most common methods of representing such networks, and how these are manipulated, is explained. The concepts of power wave S-parameters and pseudo wave S-parameters are described. Power and pseudo wave S-parameters are distinctly different to the common form of travelling wave S-parameters because they allow the performance of networks to be represented in terms of incident and reflected waves in the presence of complex port loads.

3.1 Transmission Line Theory

Transmission line theory describes the properties of electrical connections that experience voltage and current changes that vary faster than the time taken for these changes to propagate along the connections length. Therefore, the length of the connection is important when the signal includes frequency components for which the corresponding wavelengths are comparable to the length of the connection.

3.1.1 Telegraph Equations and Lumped-Element Circuit Model

The *telegraph equations* are a pair of linear differential equations, Equations (3.1) and (3.2), that describe the voltage and current on an electrical transmission line in terms of distance and time. They were developed by Oliver Heaviside who created the transmission line model, and are based on Maxwell's Equations (Heaviside 1885, Weber and Nebeker 1994).

The transmission line model represents the transmission line as an infinite series of two-port elementary components, each representing an infinitesimally short segment of the transmission line, as illustrated in Figure 3.1, where $Z = R + j\omega L$ and $Y = G + j\omega C$. The distributed resistance R of the conductors is represented by a series resistor. The distributed inductance L, due to the magnetic field around the wires, is represented by a series inductor. The capacitance C between the two conductors is represented by a shunt capacitor. The conductance G of the dielectric material separating the two conductors is represented by a conductance shunted between the signal wire and the return wire. These component values are all specified per unit length, and are functions of frequency.

The line voltage $v(z)$ and the current $i(z)$ of Figure 3.1 can be expressed in the frequency domain as:

$$\begin{aligned} \frac{\partial v(z)}{\partial z} &= -(R + j\omega L)i(z), \qquad (3.1) \\ &= -Zi(z), \\ \frac{\partial i(z)}{\partial z} &= -(G + j\omega C)v(z), \qquad (3.2) \\ &= -Yv(z), \end{aligned}$$

where the series impedance and shunt admittance per unit length is:

$$\begin{aligned} Z &= R + j\omega L, \\ Y &= G + j\omega C. \end{aligned}$$

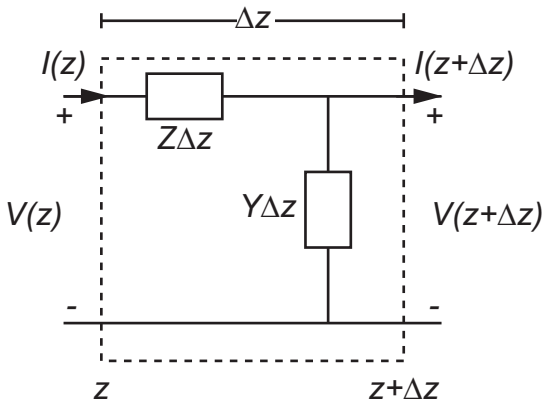

Figure 3.1: Transmission line circuits. The lumped equivalent circuit, shown here, is used to model the behaviour of a short length, Δz, of transmission line. Large transmission line circuits are modelled by replacing the transmission lines with many of these equivalent circuit elements in series. Each circuit element consists of a small series inductance and resistance, $Z_{\Delta z}$ with a shunt capacitance and conductance, $Y_{\Delta z}$.

If we eliminate i between Equations (3.1) and (3.2) we obtain

$$\frac{\partial^2 v(z)}{\partial z^2} = \gamma^2 v(z), \tag{3.3}$$

where

$$\begin{aligned} \gamma &= \sqrt{(R+j\omega L)(G+j\omega C)}, \\ &= \sqrt{ZY}, \\ &= \alpha + j\beta, \end{aligned} \tag{3.4}$$

is called the *propagation constant* (IEEE Standard 1990). The variable α is called the *attenuation constant* and the variable β is the *phase constant* (IEEE Standard 1990).

A solution of Equation (3.3) is

$$v(z) = v_f e^{-\lambda z} + v_r e^{+\lambda z}. \tag{3.5}$$

The subscripts f and r are chosen because v_f represents the amplitude and the phase of a forward propagating wave, while v_r represents the amplitude and phase of a reverse propagating wave. These are wave equations that represent waves with equal propagation speed in the forward and reverse directions.

The current $i(z)$ which accompanies this voltage can be derived from Equations (3.1) and (3.5) to be

$$i(z) = -\frac{1}{Z}\Big[-\lambda v_f e^{-\lambda z} + \lambda v_r e^{+\lambda z}\Big].$$

We substitute for λ from Equation (3.4), and obtain

$$\begin{aligned} i(z) &= \sqrt{\frac{Y}{Z}}\left[v_f e^{-\lambda z} - v_r e^{+\lambda z}\right], \\ &= \frac{1}{Z_0}\left[v_f e^{-\lambda z} - v_r e^{+\lambda z}\right], \\ &= \frac{v(z)}{Z_0}, \end{aligned}$$

where

$$\begin{aligned} Z_0 &= \sqrt{\frac{R + j\omega L}{G + j\omega C}}, \\ &= \sqrt{\frac{Z}{Y}}, \end{aligned}$$

which we call the characteristic impedance of the line. The wavelength on the line is

$$\lambda = \frac{2\pi}{\beta}$$

and the phase velocity is

$$\begin{aligned} v_p &= \frac{\omega}{\beta} \\ &= \lambda f. \end{aligned}$$

3.1.2 Reflection Coefficient and Impedance Transformation

A transmission line supports both the forward and reverse, or reflected, propagating waves. When a forward propagating wave encounters a load, a portion of the wave's energy is absorbed by the load. Unless the transmission line is perfectly matched, some of the energy is reflected back into the line, exciting the reflected wave. The relationship between the forward and reverse propagating wave is known as the *voltage reflection factor* denoted by Γ_v. At any point on a transmission line the reflection factor is

$$\Gamma_v(z) = \frac{\text{complex amplitude of the reverse voltage wave at } z}{\text{complex amplitude of the forward voltage wave at } z}.$$

For a passive circuit as depicted in Figure 3.2, the reflection coefficient is related to the transmission line characteristic impedance, Z_0 and load, Z_L, and is calculated using

$$\Gamma_v(z) = \frac{Z(z) - Z_0}{Z(z) + Z_0}. \tag{3.6}$$

In a similar way, the impedance at any point on the line is calculated from the relative forward and reverse waves using

$$\frac{Z(z)}{Z_0} = \frac{1+\Gamma_v(z)}{1-\Gamma_v(z)}. \tag{3.7}$$

In this way the load impedance is transformed by the transmission line. The input impedance, Z_I at any point on a line terminated with the load impedance Z_L is calculated using the formula

$$Z_I = \frac{Z_L \cosh \lambda l + Z_0 \sinh \lambda l}{Z_0 \cosh \lambda l + Z_L \sinh \lambda l}.$$

This result applies to a line of arbitrary length, losses, and load impedance.

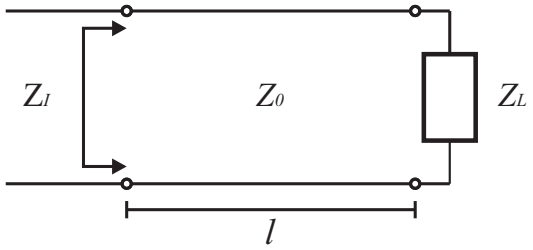

Figure 3.2: Reflection coefficient of a transmission line. The input impedance of the transmission line, Z_I, is determined by the load Z_L connected to the end of the transmission line, the length of the transmission line l and the characteristic impedance of the transmission line Z_0.

Normalised Impedance

These formulae are simplified by normalising impedances by the characteristic impedance of the transmission line. The normalised impedance z corresponding to an actual impedance Z as

$$z = \frac{Z}{Z_0}.$$

The Equations (3.6) and (3.7) above then simplify to

$$\Gamma_v = \frac{z-1}{z+1},$$

and

$$z = \frac{1+\Gamma_v}{1-\Gamma_v}.$$

This normalised z is dimensionless. It is convenient parameter to use because Γ is also dimensionless.

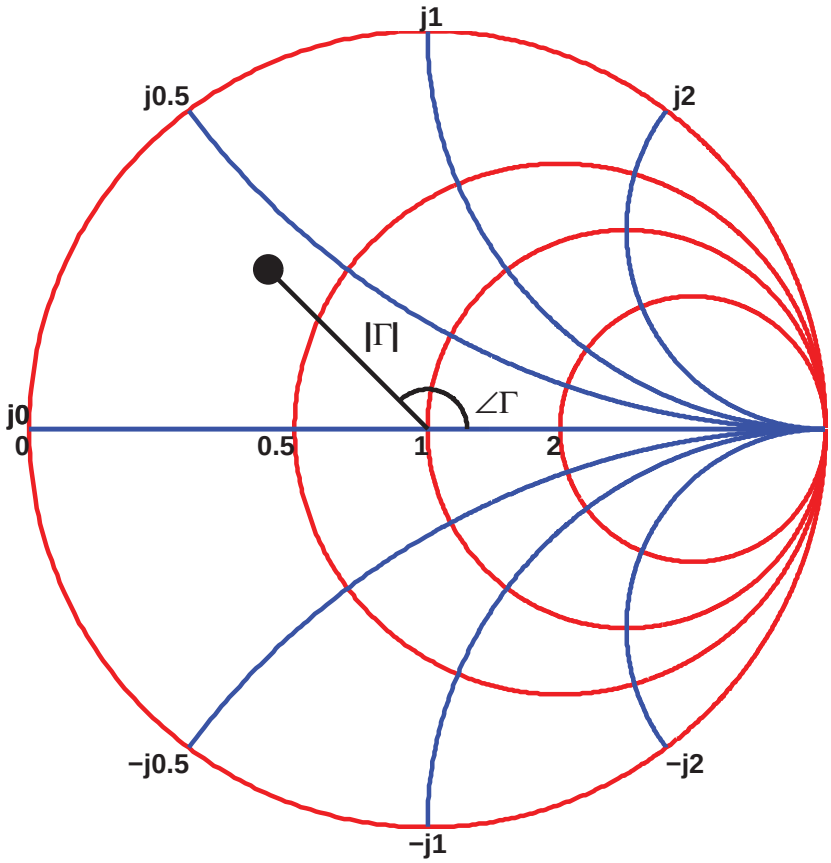

Figure 3.3: Smith chart. The Smith chart is a powerful visualisation tool. It plots polar reflection coefficients, $|\Gamma|$ and $\angle\Gamma$ on axis of real and imaginary normalised impedance or admittance. Many impedance matching networks can be represented by following the lines of constant impedance, admittance, reactance, and susceptance lines, or rotating Γ about the origin.

3.1.3 Smith Chart

The *Smith chart* provides a graphical method for the visualisation of transmission line circuits and for the solution of transmission line problems. It also provides a graphical representation of the impedance locus as a function of frequency. The Smith chart is a polar plot of Γ_v with lines of constant real and imaginary normalised impedance and/or normalised admittance (Smith 1931, Smith 1944). A normalised impedance Smith chart is shown in Figure 3.4.

The Smith chart is widely used to display S-parameters, stability circles, gain circles, and noise figure circles of microwave amplifiers. The Smith chart is also used to design and visualise matching circuits.

3.2 Network Parameters

In order to characterise the behavior of a N-port network, a number of equivalent circuit parameters have been used. At frequencies where it is possible to directly measure the voltages and currents at each port, the *impedance matrix* and *admittance matrix* are calculated. These parameters cannot be measured accurately at higher frequencies because the voltage and current can no longer be measured directly and the broadband open and shorts required become difficult to build. In the 1970's the popularity of *scattering parameters* increased because of the appearance of new network analysers that performed these measurements with ease.

3.2.1 Impedance and Admittance Matrix

The N-port network can be represented in several ways. The most common representations are the impedance matrix (Z parameters), and admittance matrix (Y parameters). These parameters are defined as:

$$\begin{aligned} v_1 &= z_{11}i_1 + z_{12}i_2 + ... + z_{1n}i_n \\ v_2 &= z_{21}i_1 + z_{22}i_2 + ... + z_{2n}i_n \\ &\vdots \\ v_n &= z_{n1}i_1 + z_{n2}i_2 + ... + z_{nn}i_n \end{aligned}$$

or in matrix form

$$\begin{bmatrix} v_1 \\ v_2 \\ \vdots \\ v_n \end{bmatrix} = \begin{bmatrix} z_{11} & z_{12} & \dots & z_{1n} \\ z_{21} & z_{22} & \dots & z_{2n} \\ \vdots & \vdots & \ddots & \vdots \\ z_{n1} & z_{n2} & \dots & z_{nn} \end{bmatrix} \begin{bmatrix} i_1 \\ i_2 \\ \vdots \\ i_n \end{bmatrix}.$$

The admittance matrix is simply the inverse of the impedance matrix, $Y = Z^{-1}$,

$$\begin{bmatrix} i_1 \\ i_2 \\ \vdots \\ i_n \end{bmatrix} = \begin{bmatrix} y_{11} & y_{12} & \dots & y_{1n} \\ y_{21} & y_{22} & \dots & y_{2n} \\ \vdots & \vdots & \ddots & \vdots \\ y_{n1} & y_{n2} & \dots & y_{nn} \end{bmatrix} \begin{bmatrix} v_1 \\ v_2 \\ \vdots \\ v_n \end{bmatrix}.$$

At microwave and millimetre wave frequencies the Z and Y parameters cannot be easily measured. Therefore, another measurement method is needed that is capable of characterising circuits at any frequency. The appropriate representation is called the *scattering matrix* and the *scattering parameters* are defined in terms of travelling waves.

3.2.2 S-Parameters Based on Travelling-Waves

Like the impedance or admittance matrix, the scattering matrix combined with its reference impedances, provides a complete description of the network. While the impedance and admittance matrices relate the voltages and currents at the ports, the scattering matrix relates the voltage waves entering the ports to those reflected from the ports (Oliner 1984). Once the scattering parameters of the network are known, conversion to other matrix parameters may be performed as required.

To correctly relate incident and reflected voltage waves to incident and reflected currents and power, the measurements at each port are conducted using a constant reference impedance. In practice, the reference impedance is generally chosen to be $Z_0 = 50\,\Omega$. The two-port scattering parameters can be measured by embedding the network in a transmission line, whose characteristic impedance is $50\,\Omega$, and connecting the ends to a network analyser.

Travelling waves refer to the unidirectional, single mode waves that form the basis for scattering matrix analysis. Circuit theory based on travelling waves describes the electromagnetic interactions of a transmission line circuit and has led to the standard methodology of handling RF and microwave problems. The scattering matrix relates the outgoing waves b_n to the incoming waves a_n that are incident on the N-port network:

$$\begin{bmatrix} b_1 \\ b_2 \\ \vdots \\ b_n \end{bmatrix} = \begin{bmatrix} S_{11} & S_{12} & \dots & S_{1n} \\ S_{21} & S_{22} & \dots & S_{2n} \\ \vdots & \vdots & \ddots & \vdots \\ S_{n1} & S_{n2} & \dots & S_{nn} \end{bmatrix} \begin{bmatrix} a_1 \\ a_2 \\ \vdots \\ a_n \end{bmatrix}. \tag{3.8}$$

The matrix elements S_{nm}, for $n = 1, 2, .., N$ are referred to as the scattering parameters or the S-parameters. The parameters S_{nn} have the same meaning as the reflection coefficient described earlier, and S_{nm}, for $n \neq m$, are the transmission coefficients.

The travelling wave variables a and b are defined in terms of v, and i and a real-valued positive reference impedance Z_0, as follows:

$$a(z) = \frac{v(z) + Z_0 i(z)}{2\sqrt{Z_0}}$$
$$b(z) = \frac{v(z) - Z_0 i(z)}{2\sqrt{Z_0}},$$

where $v(z)$ and $i(z)$ are the voltage and current at a point z along the line and Z_0 is the characteristic impedance. The reference plane is the position along the transmission line where all measurements are made, the position is defined by the variable z.

Shift of Reference Planes

S-parameters describe the incident and reflected waves on identical lossless transmission lines connected to each port of the network. Therefore, it is a simple matter to shift the reference plane of each port by any distance l.

The theory of travelling waves on a lossless transmission line allows the shifted voltage waves to be related to the unshifted voltage waves by

$$a_n = a'_n e^{-j\theta_n}$$
$$b'_n = b_n e^{-j\theta_n},$$

where $\theta = \beta_n l_n$ is the electrical length of the outward shift of the reference plane of port n. Equation (3.8) becomes

$$\begin{bmatrix} b_1 \\ b_2 \\ \vdots \\ b_n \end{bmatrix} = \begin{bmatrix} e^{-j\theta_1} & 0 & \dots & 0 \\ 0 & e^{-j\theta_2} & \dots & 0 \\ \vdots & \vdots & \ddots & \vdots \\ 0 & 0 & \dots & e^{-j\theta_n} \end{bmatrix} S \begin{bmatrix} e^{-j\theta_1} & 0 & \dots & 0 \\ 0 & e^{-j\theta_2} & \dots & 0 \\ \vdots & \vdots & \ddots & \vdots \\ 0 & 0 & \dots & e^{-j\theta_n} \end{bmatrix} \begin{bmatrix} a_1 \\ a_2 \\ \vdots \\ a_n \end{bmatrix}.$$

Therefore the shifted scattering parameters are

$$S' = \begin{bmatrix} e^{-j\theta_1} & 0 & \dots & 0 \\ 0 & e^{-j\theta_2} & \dots & 0 \\ \vdots & \vdots & \ddots & \vdots \\ 0 & 0 & \dots & e^{-j\theta_n} \end{bmatrix} S \begin{bmatrix} e^{-j\theta_1} & 0 & \dots & 0 \\ 0 & e^{-j\theta_2} & \dots & 0 \\ \vdots & \vdots & \ddots & \vdots \\ 0 & 0 & \dots & e^{-j\theta_n} \end{bmatrix}.$$

Power and Matching

Power flow into the nth-port of a network whose ports are terminated with impedance Z_0, is expressed in terms of the travelling wave amplitudes:

$$\begin{aligned} P_n &= \frac{1}{2}|a_n|^2 - \frac{1}{2}|b_n|^2, \\ &= \frac{1}{2}|a_n|^2(1 - |S_{nn}|^2). \end{aligned}$$

The maximum power that can be delivered by the generator to a connected load is called the available power of the generator, P_{av}, and is obtained when the load is conjugate-matched to the generator, that is, $P_{\text{av}} = P_{\text{in}}$ when $Z_{\text{in}} = Z_{\text{G}}^*$. Further, since the travelling wave reflection coefficient is given by:

$$\Gamma = \frac{Z_L - Z_0}{Z_L + Z_0},$$

$P_{\text{av}} = P_{\text{in}}$ when $\Gamma_{\text{in}} = \Gamma_{\text{G}}^*$. While all other ports in a n-port network are terminated in their reference impedance, a generator connected to port n experiences $\Gamma_{\text{in}} = S_{nn}$, the input impedance is then calculated using Equation (3.7). If the other ports of the network are not terminated in their reference impedance, $\Gamma_{\text{in}} \neq S_{nn}$ and Equation (3.7) is no longer appropriate. Therefore, to solve this problem using the classical travelling wave S-parameters, signal flow graphs must be used (Pozar 1998). This is a very time consuming approach that grows in complexity as the number of ports increase. A more convenient solution is to represent the system using scattering parameters with a reference impedance at each port equal to the load or generator impedance at that port $Z_{\text{ref},n}$.

3.2.3 S-Parameters Pseudo-waves

Pseudo-waves are linear combinations of travelling waves that are sometimes convenient to use *in lieu* of travelling waves. These can be referenced to an arbitrary port impedance for use in a wider range of applications. Vector network analyser calibrations and measurements for example are derived from pseudo-waves (Marks and Williams 1992, Frickey 1994, Marks et al. 1995). These are more loosely based on the electromagnetic interactions than travelling waves but are a practical abstraction for measurement and other purposes.

The pseudo-wave method is derived from the physical travelling wave analysis and has the wave variables expressed as:

$$a(z) = K\frac{\sqrt{\Re(Z_{\text{ref}})}}{2|Z_{\text{ref}}|}(v + iZ_{\text{ref}})$$
$$b(z) = K\frac{\sqrt{\Re(Z_{\text{ref}})}}{2|Z_{\text{ref}}|}(v - iZ_{\text{ref}})$$

where $\Re(Z_{\text{ref}})$ is the real component of the reference impedance Z_{ref} and K is a normalising term dependent on how voltage is measured on the transmission structure, and is unity for most cases. The real part of Z_{ref} is restricted to positive values. This results in the reflection coefficient, and its inverse, being calculated using the formulae:

$$\Gamma = \frac{Z_L - Z_{\text{ref}}}{Z_L + Z_{\text{ref}}},$$
$$Z = Z_{\text{ref}}\frac{1+\Gamma}{1-\Gamma},$$

where both are identical to the travelling wave case.

It is possible for passive pseudo S-parameters to contain coefficients greater than 1 for complex reference impedances. This leads to the less than intuitive expression for the delivered power into a port, expressed by:

$$P = |a|^2 \left[1 - |\Gamma|^2 - 2\Im(\Gamma)\frac{\Im(Z_{\text{ref}})}{\Re(Z_{\text{ref}})}\right], \tag{3.9}$$

where $\Re$ denotes the real component and $\Im$ denotes the imaginary component.

Note that Z-parameters are independent of reference impedance since they depend purely on the voltage and current at each port. While a network's S-parameters vary depending on each port's reference impedance, the Z-parameters will not vary. Conversions between pseudo-wave S-parameters and Z-parameters are governed by the following relations:

$$\begin{aligned}
\mathbf{S} &= \mathbf{U}(\mathbf{Z} - \mathbf{Z}_{\text{r}})(\mathbf{Z} + \mathbf{Z}_{\text{r}})^{-1}\mathbf{U}^{-1}, \\
\mathbf{Z} &= (\mathbf{I} - \mathbf{U}^{-1}\mathbf{S}\mathbf{U})^{-1}(\mathbf{I} + \mathbf{U}^{-1}\mathbf{S}\mathbf{U})\mathbf{Z}_{\text{r}},
\end{aligned}$$

where

$$\begin{aligned}
\mathbf{U}_{nn} &= \frac{\sqrt{\Re(\mathbf{Z}_{\text{ref},n})}}{|\mathbf{Z}_{\text{ref},n}|}, \\
\mathbf{U}_{nm} &= 0 \text{ for } n \neq m,
\end{aligned}$$

and

$$\begin{aligned}
\mathbf{Z}_{r,nn} &= \mathbf{Z}_{\text{ref},n}, \\
\mathbf{Z}_{r,nm} &= 0 \text{ for } n \neq m.
\end{aligned}$$

These equations are extended to express the power-wave S-parameters in terms of new reference impedances,

$$\mathbf{S}' = \mathbf{P}^{-1}(\mathbf{S} - \gamma)(\mathbf{I} - \gamma\mathbf{S})^{-1}\mathbf{P}, \tag{3.10}$$

$$\tag{3.11}$$

where

$$\begin{aligned}
\mathbf{P}_{nn} &= \sqrt{\frac{\Re(\mathbf{Z}'_{\text{ref},n})}{\Re(\mathbf{Z}_{\text{ref},n})}}\left|\frac{\mathbf{Z}'_{\text{ref},n}}{\mathbf{Z}_{\text{ref},n}}\right|\frac{2\mathbf{Z}_{\text{ref},n}}{\mathbf{Z}_{\text{ref},n} + \mathbf{Z}'_{\text{ref},n}}, \\
\mathbf{P}_{nm} &= 0 \text{ for } n \neq m,
\end{aligned} \tag{3.12}$$

and

$$\begin{aligned}
\gamma_{nn} &= \frac{\mathbf{Z}'_{\text{ref},n} - \mathbf{Z}_{\text{ref},n}}{\mathbf{Z}'_{\text{ref},n} + \mathbf{Z}_{\text{ref},n}}, \\
\gamma_{nm} &= 0 \text{ for } n \neq m.
\end{aligned}$$

Here the original S-parameters and reference impedances are denoted by $\mathbf{S}$ and $\mathbf{Z}_{\text{ref}}$ and the new ones by $\mathbf{S}'$ and $\mathbf{Z}'_{\text{ref}}$.

3.2.4 S-Parameters Based on Power-Waves

The travelling-wave and pseudo-wave concept is more closely related to the voltage or current along the line than to the power in a stationary state. If a circuit that terminates a transmission line at the far end is not matched to the characteristic impedance of the line, even if the circuit has no source at all, two waves travelling in opposite directions along the line must be considered.

In contrast to both pseudo-waves and travelling waves, power-waves do not represent the electromagnetic interactions at all. Instead they are derived as if the voltages and currents associated with the waves are already known. Like pseudo-waves, the power-waves make use of a port reference impedance, however the implications are quite different (Kurokawa 1965).

These wave-like variables can no longer be interpreted as incoming and outgoing waves from the two sides of the two-port. However they have a convenient interpretation in terms of power transfer and simplify the expressions for the power gains. The power wave construct expresses the incident and reflected wave-like variables as:

$$a(z) = \frac{1}{2\sqrt{\Re(Z_{\text{ref}})}}(v + iZ_{\text{ref}})$$
$$b(z) = \frac{1}{2\sqrt{\Re(Z_{\text{ref}})}}(v - iZ^*_{\text{ref}}).$$

This results in the reflection coefficient being calculated using the formula:

$$\Gamma = \frac{Z_L - Z^*_{\text{ref}}}{Z_L + Z_{\text{ref}}}.$$

Note the presence of the conjugate of the reference impedance. In contrast to travelling-waves and pseudo-waves, the reflection coefficient becomes zero when $Z_L = Z^*_{\text{ref}}$ for complex values. The inverse relation used to calculate the load impedance from Γ is a little more complicated:

$$\begin{aligned} Z_L &= \Re(Z_{\text{ref}})\Re(z) + j(\Re(Z_{\text{ref}})\Im(z) - \Im(Z_{\text{ref}})), \\ z &= \frac{1 + S_{nn}}{1 - S_{nn}}. \end{aligned}$$

As stated earlier, the delivered power is expressed very simply by:

$$P = |a|^2 - |b|^2.$$

Conversions to and from Z-parameters is governed by the following relations:

$$\begin{aligned} \mathbf{S} &= \mathbf{F}(\mathbf{Z} - \mathbf{Z}^*_r)(\mathbf{Z} + \mathbf{Z}_r)^{-1}\mathbf{F}^{-1}, \\ \mathbf{Z} &= \mathbf{F}^{-1}(\mathbf{I} - \mathbf{S})^{-1}(\mathbf{S}\mathbf{Z}_r + \mathbf{Z}^*_r)\mathbf{F}, \end{aligned}$$

where

$$\begin{aligned}\mathbf{F}_{nn} &= \frac{1}{2\sqrt{|\Re(\mathbf{Z}_{\mathrm{ref},n})|}},\\ \mathbf{F}_{nm} &= 0 \text{ for } n \neq m,\end{aligned}$$

and

$$\begin{aligned}\mathbf{Z}_{r,nn} &= \mathbf{Z}_{\mathrm{ref},n},\\ \mathbf{Z}_{r,nm} &= 0 \text{ for } n \neq m.\end{aligned}$$

Again, these equations have been extended to express the pseudo wave S-parameters in terms of new reference impedances,

$$\mathbf{S}' = \mathbf{Q}^{-1}(\mathbf{S}-\mathbf{\Gamma}^*)(\mathbf{I}-\mathbf{\Gamma},\mathbf{S})^{-1}\mathbf{Q}^*,$$

where

$$\begin{aligned}\mathbf{Q}_{nn} &= \sqrt{\left|\frac{\Re(\mathbf{Z}'_{\mathrm{ref},n})}{\Re(\mathbf{Z}_{\mathrm{ref},n})}\right|}\frac{\mathbf{Z}_{\mathrm{ref},n}+\mathbf{Z}^*_{\mathrm{ref},n}}{\mathbf{Z}'^*_{\mathrm{ref},n}+\mathbf{Z}_{\mathrm{ref},n}},\\ \mathbf{Q}_{nm} &= 0 \text{ for } n \neq m,\end{aligned}$$

and

$$\begin{aligned}\mathbf{\Gamma}_{nn} &= \frac{\mathbf{Z}'_{\mathrm{ref},n}-\mathbf{Z}_{\mathrm{ref},n}}{\mathbf{Z}'_{\mathrm{ref},n}+\mathbf{Z}^*_{\mathrm{ref},n}},\\ \mathbf{\Gamma}_{nm} &= 0 \text{ for } n \neq m.\end{aligned}$$

3.2.5 Summary

To match each port of a constrained lens the load at each port is varied until maximum power transfer is achieved. This is carried out by changing the reference impedance at each port and renormalising the S-parameters to show the new behaviour of the lens. This cannot be carried out using travelling-wave S-parameters and therefore pseudo-wave or power-wave S-parameters must be used.

When Z_{ref} is real, the three definitions are identical. However, there are differences between the pseudo-wave and power-wave definitions when Z_{ref} is complex. These differences manifest themselves in the power transfer equations, Smith chart geometry, and transfer matrix behaviour.

The expression for power transfer for the pseudo-wave computation is not intuitive if Z_{ref} is not real:

$$P = |a|^2 \left[1 - |\Gamma|^2 - 2\Im(\Gamma)\frac{\Im(Z_{\text{ref}})}{\Re(Z_{\text{ref}})}\right].$$

This means that it is possible for $|\Gamma|$ to be greater than 1 for a passive device if the reference impedance is not real. The third term allows this without violating conservation of energy. In contrast, power wave formulation has a very simple expression for delivered power:

$$\begin{aligned} P &= |a|^2 - |b|^2 \\ &= |a|\left[1 - |\Gamma|^2\right]. \end{aligned}$$

The pseudo-wave formulation of the Smith chart behaves in much the same way as for the travelling wave. Figure 3.4(a) shows that like the travelling wave Smith chart, the magnitude of the reflection coefficient will be zero if the input impedance is equal to the reference impedance. Further, the open and short circuit will also correspond to reflection coefficients of 1 and -1. However, the lines of constant resistance and admittance are significantly different. The Smith chart appears to be enlarged and moved but it is interesting to note that the complex conjugate of the reference impedance still appears in the centre of the chart. These unusual properties are because $|\Gamma|$ is allowed to be greater than unity for a passive element.

The power-wave plot of the Smith chart is shown in Figure 3.4(b). While it appears to resemble the travelling wave Smith chart, there are significant differences. The reflection coefficient is no longer zero if the input impedance is equal to the reference impedance. Instead, it is the complex conjugate of the reference impedance that reduces the reflection coefficient to zero. This corresponds to the impedance required to achieve maximum power transfer. Closer inspection reveals that while the open circuit will be represented by a reflection coefficient of 1, a short will be represented by:

$$\Gamma_{\text{short}} = \frac{-Z_{\text{ref}}^*}{Z_{\text{ref}}}.$$

Transfer matrices are not used in this thesis, however, they are an important computational tool that is often used with travelling wave scattering parameters. Transfer matrices behave quite differently in the two S-parameter formulations. The process of multiplying two such matrices works in the pseudo-wave formulation in the same way that travelling wave formulation does. In both these cases, the output port reference impedance of the

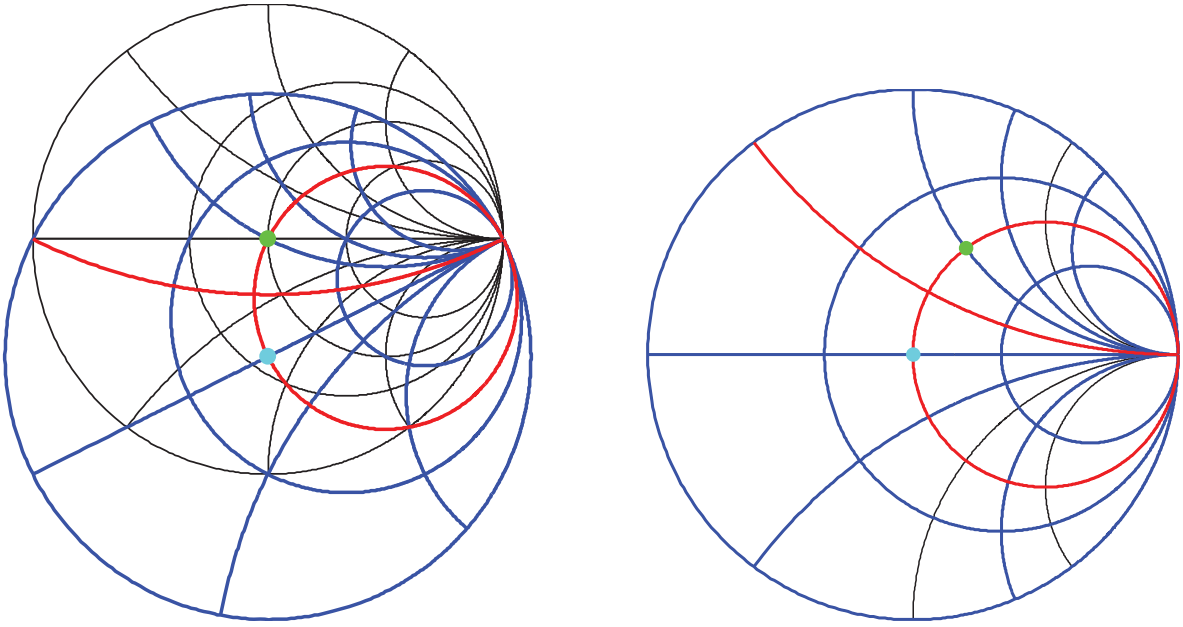

(a) Pseudo wave (b) Power wave

Fig. 3.4: Pseudo and power Smith chart. The Smith chart has been replotted using the pseudo wave definition for reflection coefficient, Subfigure (a), and the power wave reflection coefficient, Subfigure (b). A reference impedance of $1 + 0.5j$ is shown on each plot by the green dot. The load required for maximum power transfer is the complex conjugate, and the position of this load is shown by the blue dot. The original Smith chart with real Z_0, reference impedance of 1, is shown in black. The $\Im(Z) = 0$ and $\Re(Z) = 1$ lines are shown in red. Like the standard Smith chart, the pseudo wave definition places the open circuit at $1\angle 0$ and reference impedance at 0. In contrast, the magnitude of the reflection coefficient becomes greater than one for some loads. The power wave definition places the load required for maximum power transfer at the origin and $|\Gamma| \leq 1$ for all passive networks.

first set of S-parameters must be equal to that of the input port of the second set of S-parameters. In the power wave construct, one must be the complex conjugate of the other.

Linear multi-port networks are characterised by a number of equivalent circuit parameters, such as their transfer matrix, impedance matrix, admittance matrix, and scattering matrix. Scattering parameters based on travelling waves do not facilitate matching such a complex system. Instead pseudo-wave and power-wave allow S-parameters to be expressed in terms of the load impedance of each port. This greatly simplifies the optimisation of the system. The power-wave representation also simplifies the representation of power

flow to and from the n-port network. These reasons make power-waves the obvious choice for the design and optimisation of constrained lenses.

3.3 Impedance Matching Circuits

Impedance matching is used to ensure maximum power from a generator is transferred to the load. The condition that achieves maximum power transfer from generator to load is know as *conjugate matching*. This means that the load seen by the generator, Z_{in}, is the complex conjugate of the generator impedance,

$$Z_{\text{in}} = Z_G^*.$$

If the load and generator are connected together using a transmission line, two matching networks are generally used to match both to the characteristic impedance of the transmission line. This means that the forward propagating wave excited by the generator does not excite a reverse propagating wave at the interface of the load matching network. This is known as *reflectionless matching* because no energy is reflected from either end of the line. Therefore, the length of the interconnecting transmission line can be varied without effecting the behaviour of the system. In general, both generator and load need not be matched to the transmission line. In this case, the condition for maximum power transfer from the generator to the load will excite reflections at both ends of the line and a standing wave will be present.

The following section will give an overview of transmission line based impedance matching networks that are useful for the design of constrained lenses at microwave frequencies. Series transmission line matching networks are used because they are easily implemented, in a confined space, in the same process as the microstrip or stripline constrained lens.

3.3.1 Quarter-Wavelength Transformers

The quarter wavelength transformer is the basic building block of transmission line matching. It is well known and widely used as a narrow-band matching network between real impedances.

The quarter wavelength transformer matches two real impedances, R_1 and R_2, with a quarter wavelength transmission line having characteristic impedance Z_0. The well-known

equation, describing the relationship between these three variables and the length of the transmission line l (Orfanidis 2008), is

$$\frac{R_1}{Z_O} = \frac{R_2 \cos \beta l + j Z_O \sin \beta l}{Z_O \cos \beta l + j R_2 \sin \beta l}.$$

When $l = \frac{\lambda}{4}$, $\beta l = \frac{\pi}{2}$, and the above equation reduces to

$$R_1 = \frac{Z_O^2}{R_2}.$$

By not restricting the length of the series transmission line to $\frac{\lambda}{4}$, the series transmission line transforms between two complex impedances.

3.3.2 Series Transformer

The series impedance transformer is the generalised form of the quarter wavelength transformer but is rarely mentioned in text books. The characteristic impedance of the series section line needed to match a complex load to a real impedance has been reported (Balabanian 1955, French and Fooks 1968) and the benefits of using a series transformer compared to a series line followed by a quarter wavelength transformer has been demonstrated (Hamid and Yunik 1967). However, a general solution that allows matching between two complex impedances, and its solution space, has only briefly been presented (Rosloniec 1994).

The series transformer that matches two impedances, Z_1 and Z_2, with a length of transmission line l, having characteristic impedance Z_O, is shown in Figure 3.5. The equation describing the relationship between these four variables (Orfanidis 2008), is

$$\frac{Z_1}{Z_O} = \frac{Z_2 \cos \beta l + j Z_O \sin \beta l}{Z_O \cos \beta l + j Z_2 \sin \beta l}.$$

The expression for determining the characteristic impedance Z_O, and the length of the line l matching Z_1, and Z_2, is presented as follows.

Characteristic impedance formulae

The reflection coefficients of Z_1 and Z_2, when connected to the transmission line with characteristic impedance Z_O, are given by the following formulae:

$$\Gamma_1 = \frac{Z_1 - Z_O}{Z_1 + Z_O}, \tag{3.13}$$

$$\Gamma_2 = \frac{Z_2 - Z_O}{Z_2 + Z_O}. \tag{3.14}$$

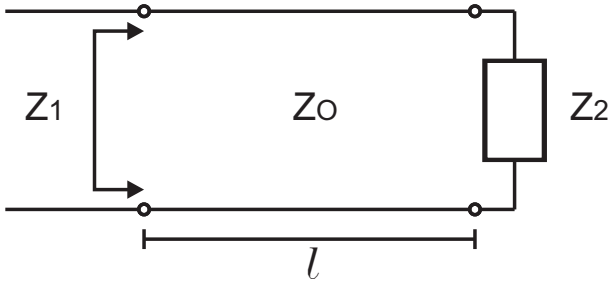

Figure 3.5: Series connected transmission line. The quarter wavelength impedance transformer matches two real impedances by a $\lambda/4$ length of transmission line. The quarter wavelength transformer is an example of the series impedance transformer. The series impedance transformer matches two complex impedances, Z_1 and Z_2 using a single section of transmission line with characteristic impedance Z_0 and length l.

Substituting Z_1 and Z_2 with their real and imaginary parts,

$$Z_1 = R_1 + jX_1, \tag{3.15}$$

$$Z_2 = R_2 + jX_2, \tag{3.16}$$

and noting that for the matched case, the magnitude of Γ_1 and Γ_2 will be equal, ie. $|\Gamma_1|^2 = |\Gamma_2|^2$, then

$$\frac{(R_1 - Z_O)^2 + X_1^2}{(R_1 + Z_O)^2 + X_1^2} = \frac{(R_2 - Z_O)^2 + X_2^2}{(R_2 + Z_O)^2 + X_2^2}$$

follows. This expression rearranges to

$$Z_O^2 = \frac{R_2(R_1^2 + X_1^2) - R_1(R_2^2 + X_2^2)}{R_1 - R_2}, \tag{3.17}$$

demonstrating that it is possible to transform from Z_1 to Z_2 with a transmission line of characteristic impedance Z_0, provided Z_0 is real. Calculating Γ_1 and Γ_2 using Equations (3.13) and (3.14), the length of the line is obtained from

$$e^{j2\beta l} = \frac{\Gamma_1}{\Gamma_2}. \tag{3.18}$$

If Z_0 is complex, this circuit cannot be implemented and other techniques must be used. A viable solution exists if

$$R_2 > R_1 \quad \text{and} \quad \frac{R_2}{|Z_2|^2} < \frac{R_1}{|Z_1|^2},$$

or

$$R_2 < R_1 \quad \text{and} \quad \frac{R_2}{|Z_2|^2} > \frac{R_1}{|Z_1|^2}.$$

In the case that Z_1 is real ($X_1 = 0$),

$$Z_O = \sqrt{R_1\left(R_2 + \frac{X_2^2}{R_2 - R_1}\right)},$$

and a solution exists if $R_2 > R_1$ or

$$R_2 < R_1 \quad \text{and} \quad \left(R_2 - \frac{R_1}{2}\right)^2 + X_2^2 < \frac{R_1^2}{4}.$$

In the case where Z_1 is complex, the solution space is a circle of radius $\frac{|Z_1|^2}{2R_1}$ instead of $\frac{R_1}{2}$ and hence intersects the R_1 line at $\pm X_1$.In the case that $X_2 = X_1 = X$ then the solution is $Z_O = \sqrt{R_1 R_2 - X^2}$.

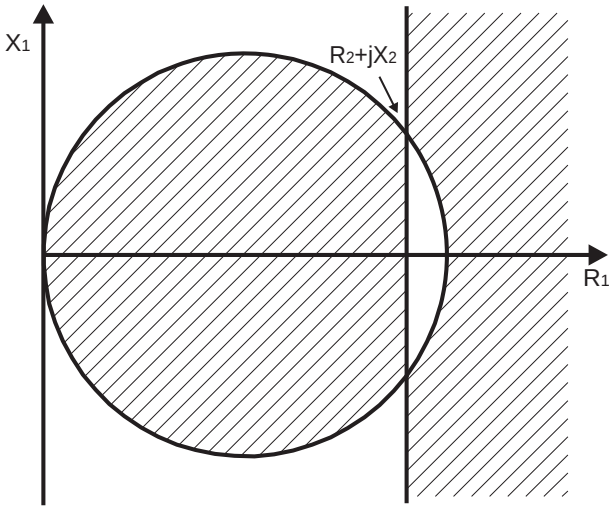

Figure 3.6: Solution space of the series impedance transformer. The series impedance transformer cannot be used to match between any two impedances. The hatched area shows the range of input impedances, $Z_1 = R_1 + jX_1$, that can be achieved using a series impedance transformer connected to a load of $Z_2 = R_2 + X_2 j$. The hatched area is inside a circle, connecting the origin and $R_2 \pm jX_2$, and less than R_2. The remaining hatched area is outside of the circle and greater than R_2.

Characteristic Admittance Formulae

In terms of admittances, Equations (3.13) and (3.14) become

$$\begin{aligned} \Gamma_1 &= \frac{Y_O - Y_1}{Y_O + Y_1}, \\ \Gamma_2 &= \frac{Y_O - Y_2}{Y_O + Y_2}, \end{aligned}$$

Equations (3.15) and (3.16) become $Y_1 = G_1 + jB_1$ and $Y_2 = G_2 + jB_2$. Similarly,

$$Y_O^2 = \frac{G_2(G_1^2 + B_1^2) - G_1(G_2^2 + B_2^2)}{G_1 - G_2},$$

replaces Equations (3.17) and (3.18) in the same way to yield the line length l.

A solution exists if

$$G_2 > G_1 \quad \text{and} \quad \frac{G_2}{|Y_2|^2} < \frac{G_1}{|Y_1|^2},$$

or

$$G_2 < G_1 \quad \text{and} \quad \frac{G_2}{|Y_2|^2} > \frac{G_1}{|Y_1|^2}.$$

These are the same solutions as for the impedance case but with R replaced by G, and X replaced by B.

3.3.3 Multi-section Impedance Transformers

The series impedance transformers described above achieve an acceptable impedance match for a narrow frequency band. Multi-section impedance transformers such as the Chebyshev and binomial impedance transformers (Solymar 1958, Young 1962), consist of a number of transmission line lengths connected in series. They both act as a bandpass filter, where each length is a quarter wavelength at the centre frequency of the pass band. The number of sections is increased to improve the reflection coefficient or increase the bandwidth of the matching network.

The binomial impedance transformer is *maximally flat*, this means that the impedance of each quarter wavelength segment is chosen to minimise the change in reflection coefficient around the centre frequency. With increasing number of line segments the reflection coefficient changes more slowly and therefore the impedance match and bandwidth is improved. An example of two, four and six segment matching networks are shown in Figure 3.7 (Riblet 1960, Young 1960, Young 1962, Gledhill 1969b, Gledhill 1969a, Gledhill 1970). As expected, the reflection coefficient becomes that of the direct impedance connection at DC and twice the centre frequency. This corresponds to when the line segment length becomes electromagnetically short, and when the line segments become half wavelength.

A Chebyshev multi-section impedance transformer can provide larger bandwidths than a binomial multi-section impedance transformer for the same number of transmission line

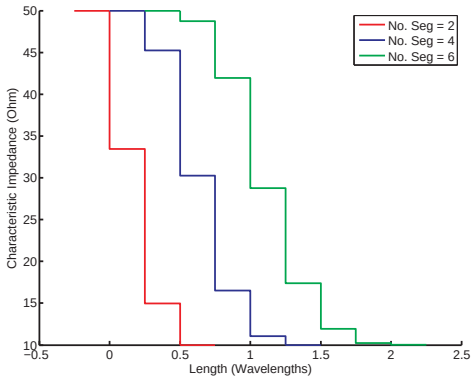

(a) Z_0 and Length

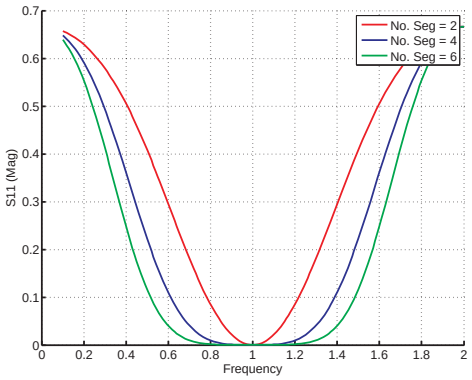

(b) Reflection Coefficient

Fig. 3.7: Binomial impedance taper performance. Three binomial impedance matching networks are shown here that transform between 10 Ω and 50 Ω. The characteristic of the binomial matching network is a smooth pass-band and higher bandwidth is achieved at the expense of length. Subfigure (a) shows the variation in transmission line characteristic impedance along the length of the three impedance transformers. Subfigure (b) clearly shows the bandwidth improvement as the number of quarter wavelength sections is increased.

sections. The increased bandwidth of the Chebyshev transformer comes at the cost of increased ripple over the networks pass-band. The Chebyshev multi-section impedance transformer behaviour is shown in Figure 3.8 for 2, 4 and 6 line segments and constant bandwidth of 1. The number of segments improves the reflection coefficient across the pass band defined in the design equations (Cohn 1955, Young 1959, Riblet 1965, Levy 1965, Orfanidis 2008).

Multi-segment impedance transformers are often used to implement bandpass filters. The Chebyshev transformer is well suited to this task because the bandwidth is defined in the design equations. The steepness of the cutoff is defined by the number of elements and the out of band rejection is equal to $(Z_L - Z_0)/(Z_L + Z_0)$.

3.3.4 Impedance Tapers

While single and multi-section quarter wavelength impedance transformers exhibit a band-pass frequency response, an *impedance taper* exhibits a high pass frequency response. An impedance taper is a smooth characteristic impedance change along the length of the transmission line, connecting two real impedances. The taper function, $Z_0(z)$, is commonly the linear (Matsumaru 1958), exponential (Wheeler 1939), Hecken (Hecken 1972,

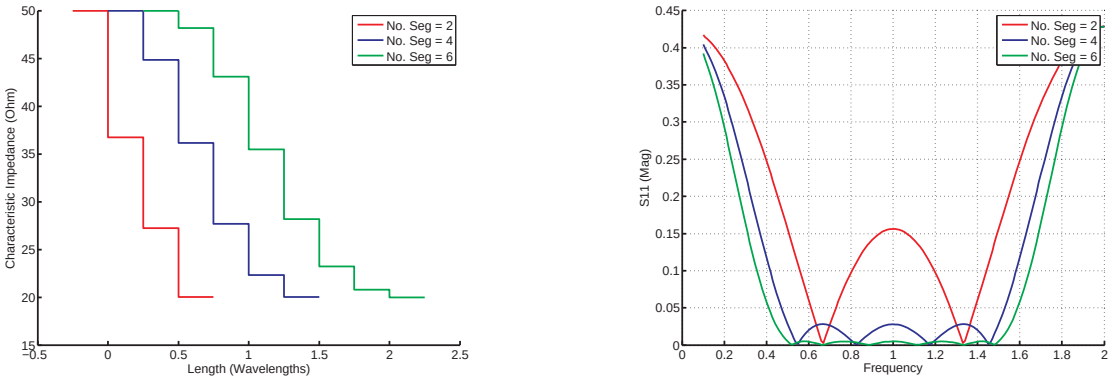

(a) Z_0 and Length

(b) Reflection Coefficient

Fig. 3.8: Chebyshev impedance taper performance. Three Chebyshev impedance matching networks are shown here that transform between 10 Ω and 50 Ω. The Chebyshev matching network is optimal in the sense that it achieves the broadest bandwidth for a given number of segments and maximum return loss. Subfigure (a) shows the variation in transmission line characteristic impedance along the length of the three impedance transformers. Subfigure (b) clearly shows the bandwidth improvement as the number of quarter wavelength sections is increased.

Hecken and Anuff 1973) (not shown), or Klopfenstein (Klopfenstein 1956, Kajfez and Prewitt 1973, Razmafrouz et al. 1996) taper seen in Figure 3.9. If the length of the taper is large, and the low frequency cut off is not important, a good match will be achieved using a linear physical taper leaving $Z_0(z)$ to be defined by the physical properties of the transmission line.

An exponential impedance taper is a half-wavelength line, at the lowest frequency of operation, whose impedance varies in an exponential fashion between the load and source impedance. The exponential taper function is expressed by:

$$Z_0(z) = Z_0 e^{az},$$

where

$$a = \frac{1}{L}\ln(\frac{Z_L}{Z_0}).$$

The exponential impedance taper does not have a step in characteristic impedance at the beginning or end of the taper ensuring a smooth transmission line. The first null appears at the frequency with a wavelength twice the length of the taper. The simple taper function of the exponential taper, absence of steps in characteristic impedance, and convenient high-pass properties produce a simple and effective transition.

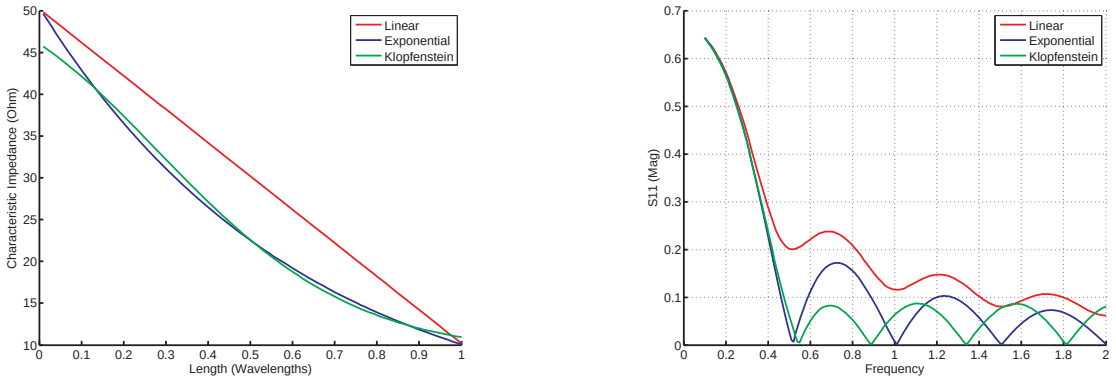

(a) Z_0 and Length

(b) Reflection Coefficient

Fig. 3.9: Impedance taper performance. Three continuous impedance tapers, between $10\ \Omega$ and $50\ \Omega$, are shown here. Subfigure (a) shows the variation of Z_0 with position. While the linear and exponential tapers begin and end at $50\,\Omega$ and $10\,\Omega$, the Klopfenstein taper has an impedance discontinuity at each end. Subfigure (b) demonstrates the poor performance of the linear taper compared to the exponential and Klopfenstein tapers. While the exponential achieves a perfect match at every multiple of $F_0/2$, the first return loss lobe may be significant. The Klopfenstein taper is optimal in the sense that the return loss drops below a given value at at the lowest possible frequency for a fixed taper length.

The Klopfenstein taper is an optimum impedance transformer that is widely used in the design of couplers, baluns and mixers (Grossberg 1968). The performance of this taper is optimum in the sense that for a fixed taper length the input reflection coefficient has minimum magnitude throughout the pass band, and for a specified maximum reflection coefficient magnitude the taper has minimum length (Klopfenstein 1956). The Klopfenstein taper is expressed by:

$$Z_0(z) \;=\; \exp\left(\frac{1}{2}\ln(Z_1 Z_2) + \frac{\frac{1}{2}\ln(\frac{Z_2}{Z_1})}{\cosh(A)}\left(A^2\phi(\frac{2x}{L}, A)\right)\right),$$

where

$$\phi(z, A) \;=\; -\,\phi(-z, A) \;=\; \int_0^z \frac{I_1(A\sqrt{1-y^2})}{A\sqrt{1-y^2}}dy,$$

for $|z| \leq 1$, and I_1 is a first order modified Bessel function of the first kind, and A is calculated using:

$$\cosh(A) \;=\; \frac{\Gamma_{\mathrm{DC}}}{\Gamma_{\mathrm{max}}}.$$

The parameter A defines the difference between the DC reflection coefficient, Γ_{DC}, and the maximum reflection coefficient in the pass band, Γ_{max}. The length of the taper, L, moves

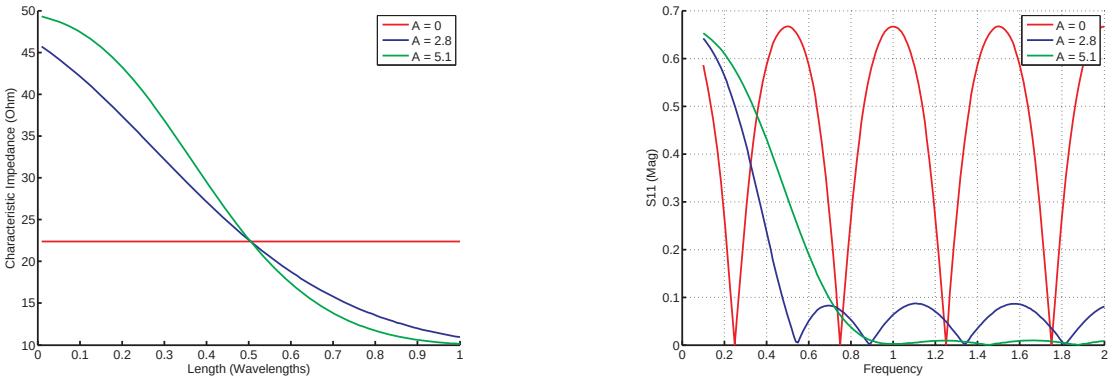

(a) Z_0 and Length

(b) Reflection Coefficient

Fig. 3.10: Klopfenstein impedance taper design. Three Klopfenstein impedance tapers, with varying values of A, are shown here. By setting $A = 0$ the taper is reduced to length of transmission line with same characteristic impedance as a quarter wavelength transformer. At higher values of A the magnitude of the minimum return loss is reduced at the expense of low frequency performance. Subfigure (a) shows the variation of Z_0 with position. Subfigure (b) demonstrates the improvement in S_{11} as A is increased, while the frequency of the first minima also increases.

the low frequency cut off of the impedance transformer. Figure 3.10 demonstrates the effect of A for a constant length taper. An interesting observation is that the Klopfenstein taper reduces to a quarter wavelength transformer for $A = 0$. Further, as $\Gamma_{\max}$ is reduced the characteristic impedance step at each end of the taper is reduced and the frequency of the first null increases.

3.3.5 Summary

Series matching networks must be used to match the closely spaced ports of a constrained lens. Complex port loads are implemented using the series transformer supplemented by an extra line segment if required. Real port loads are most compactly implemented using a quarter wavelength transformer for very narrow-band designs. The medium bandwidth lens should use binomial or Chebyshev multi-section quarter wavelength impedance transformers since they double as band-pass filters. Extreme bandwidth dictates the use of exponential or Klopfenstein tapers since they act as a high-pass filter. The minimum size of these tapers is decided by the performance of the lowest frequency of interest.

3.4 Chapter Summary

Network theory is used to represent the interactions between the Rotman lens, transmission lines, and antenna elements. S-parameter representation is ideally suited to high frequency lens designs. S-parameters are easily manipulated to determine lens beamforming performance, insertion loss, and return loss. S-parameters and network theory are fundamental tools in the design and analysis of constrained lenses.

To maximise the performance and bandwidth of the lenses described in Chapter 7, the load of each transmission line connected to the lens must be precisely defined. The desired port impedances have been found using the power-wave formulation to express the S-parameters in terms of arbitrary complex port impedances. Having defined the load impedance required at each port, matching networks are employed to transform this impedance to the characteristic impedance of the interconnecting transmission line. This chapter has presented a number of transmission line matching networks useful in this role. Before a detailed description of lens construction techniques can be presented, a review of the theory and techniques available in the literature is summarised in the following chapter.

Chapter 4

Rotman Lens Review

THIS chapter describes the operation of the Rotman lens and introduces the variables and equations that define its shape and size. Three methods for predicting the performance of the Rotman lens are presented. The first, ray optics, represents each port as an independent point source. Ray optics underpins the Rotman equations and is the most simplistic of the three methods. The second, two dimensional aperture theory replaces each point source with a two dimensional aperture antenna. This is carried out in an attempt to more realistically model the coupling between ports. Finally, electromagnetic simulation is used to predict the impact of port geometry on lens performance and to correctly account for the interaction of incident and reflected waves at every point within the lens.

These three models have been used to improve the performance of the Rotman lens. Significant advancements have been made in the design of the antenna and beam ports. This has lead to the development of low sidelobe lens designs and improved understanding of port matching and sidewall design. The chapter ends with a description of the Rotman lens applications and advancements presented in the literature.

4.1 Introduction

Lens design relies on modelling in order to replicate the performance of the lens to some degree of accuracy. This thesis considers three modelling approaches. Each successive model is more complex, but is also a more accurate representation of the physical device.

A *geometrical optics model* assumes that each port is connected to all other ports with unity magnitude and a time delay proportional to the distance between the two ports of interest. The geometrical optics model is used to optimise the:

- size of the lens relative to the aperture size,
- shape of the lens,
- length of the antenna delay lines, and
- idealised path length error.

The *two dimensional aperture model* treats each port as a two dimensional antenna with an aperture equal to the port width. In this way the coupling coefficient between any two ports is calculated. This model is used to optimise the:

- width and orientation of each port,
- excitation taper across array aperture,
- peak gain and sidelobes associated with each beam,
- insertion loss of each beam port, and
- idealised efficiency of the lens.

An *electromagnetic model* is used to accurately simulate the final structure. The accuracy of these simulations vary depending on the software and the proficiency of the user. The electromagnetic model is used to accurately predict:

- reflections within the body of the lens,
- port impedances and matching,
- mutual coupling between ports,

- coupling between delay lines,
- the optimal shape of the lens sidewalls,
- the effect of manufacturing variations,
- the performance of transmission line transitions, and
- beam pattern and mutual coupling of antenna elements.

The following sections will describe each of these three models in detail.

4.2 Geometrical Optics Model

The Rotman equations are based on geometrical optics. This approach assumes that a beam port and antenna port are connected by a single direct path. The coupling coefficient between a beam port and all antenna ports is assumed to be equal. Finally, all energy leaving a beam port is assumed to be coupled to the antenna ports resulting in a lens with no loss. In practice these assumptions are all idealisations that are impossible to achieve.

The geometrical optics, or path length model, has been used extensively to compare the optimal performance of constrained lenses. The path length from each beam port through the lens to the antenna element is calculated, as shown in Figure 4.1(a). If a beam port at position A is a perfect focal point, the path length will be a linear function of antenna element position. For all other points on the focal arc, the path length will not be a linear function of antenna element position. The deviations from the expected linear relation are referred to as *path length errors* or *aberrations*.

A typical wavefront aberration curve produced by a Rotman lens is shown in Figure 4.1(b) for a number of positions on the focal arc. The aberration curve is obtained by computing the difference between the wavefront as it leaves the array aperture and the expected ideal linear wavefront. The path-length difference is normalised relative to the focal length F. The accepted measure of path length error of a Rotman lens is the maximum deviation of this curve (Rotman and Turner 1963).

The normalisation of path length error by the focal length is not suited to optimisation of the Rotman lens as a linear antenna array feed. In this role, the path length errors scale with aperture size, not focal length. It is more appropriate then, to normalise the path length errors by the aperture size. Further, characterising the path length error by the

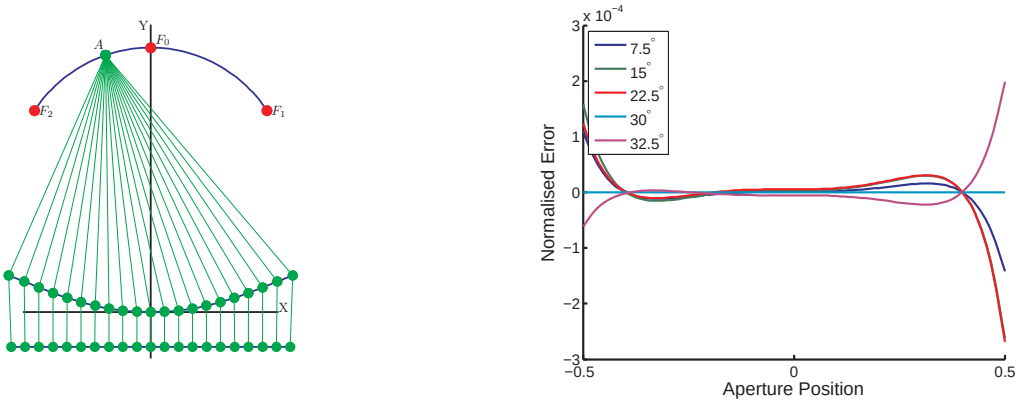

(a) Geometrical optics model.

(b) Typical aberration curves.

Fig. 4.1: Geometrical optics model and aberrations. The geometrical optics model uses the ray paths between each beam port and all antenna ports to calculate the phase performance of the Rotman lens. The ray paths of a single beam port are shown in Subfigure (a). Aberrations are the deviation of the phase of each antenna port from that of the ideal wavefront. Typical aberration curves associated with different positions on the focal arc are shown in Subfigure (b).

maximum deviation at any single element does not differentiate between beam pointing error and higher order errors. Beam pointing errors are easily corrected by moving the beam port along the focal arc, and higher order errors cannot be removed by geometrical optimisation. It is the higher order errors that are the true limitation of the Rotman lens and an error analysis that identifies this would significantly improve the selection of optimal lens variables.

The geometrical optics model only gives information about the phase of the signal at each element of the antenna array. This model does not predict port coupling or magnitude of the antenna excitation. These effects are predicted using the two dimensional aperture model described in Section 4.3.1.

4.2.1 The Rotman Lens Design Equations

The Rotman lens design equations are provided by the geometric optics model. To correctly achieve beam-forming, the Rotman lens path length equality must be satisfied. The path length equality requires that all paths, originating at one of the three perfect focal points and terminating in a planar wave, be equal in length. Each path is a sum of three lengths: the distance between beam port and antenna port through the body of the lens,

the length of the transmission line segment, and the free space distance from the antenna element to the planar wavefront. The Rotman lens geometry in Figure 4.2 shows the parameters used to define the lens. The lens geometry is defined by the position of the three focal points and the width of the lens contour. The input variables are the position of each antenna element, N, and the position of the perfect focal points specified by α, F and G. The solution results in expressions for the antenna port locations $P(X, Y)$ and each transmission line length W. The focal arc is chosen to be circular, connecting the three focal points.

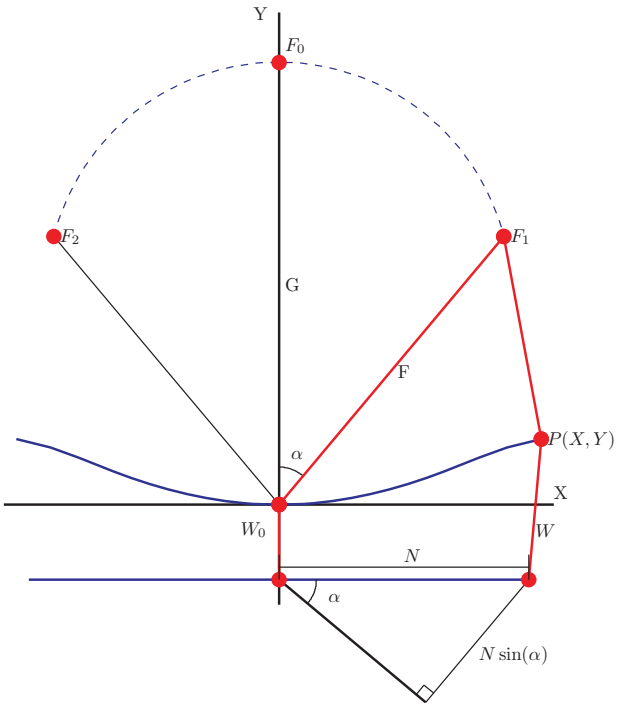

Figure 4.2: Rotman lens geometry. The array arc of the Rotman lens, $P(X, Y)$, is calculated based on the angle and distance, α and F, of the outer perfect focal point, and the distance, G, of the central focal point. Antenna ports are placed on the array arc and connected to the corresponding antenna element by a transmission line of length W. A circular wavefront with its origin at F_1 will propagate through the body of the Rotman lens producing a delay/advance of $N\sin(\alpha)$ at antenna element distance N from the origin.

Antenna Port Positions and Delays

The two off axis focal points are located a distance F from the origin and angle α from the axis, and the the third focal point is located on the axis at a distance G from the origin. The three focal points will produce plane wave fronts directed at angles α, $-\alpha$, and $0°$. The equations for optical path-length equality between the ray passing through the point $P(X,Y)$ and the ray through the origin are

$$\begin{aligned} \overrightarrow{F_1P} + W + N\sin(\alpha) &= F + W_0, & (4.1)\\ \overrightarrow{F_2P} + W - N\sin(\alpha) &= F + W_0, & (4.2) \end{aligned}$$

and

$$\overrightarrow{F_0P} + W = G + W_0, \quad (4.3)$$

where

$$\begin{aligned} (\overrightarrow{F_1P})^2 &= (F\cos(\alpha) - Y)^2 + (F\sin(\alpha) - X)^2, \\ &= F^2 + Y^2 + X^2 - 2FY\cos(\alpha) - 2FX\sin(\alpha), & (4.4)\\ (\overrightarrow{F_2P})^2 &= (F\cos(\alpha) - Y)^2 + (F\sin(\alpha) + X)^2, \\ &= F^2 + Y^2 + X^2 - 2FY\cos(\alpha) + 2FX\sin(\alpha), & (4.5) \end{aligned}$$

and

$$(\overrightarrow{F_0P})^2 = (G - Y)^2 + X^2. \quad (4.6)$$

By normalising N, X, Y, $(W - W_0)$ and G relative to the focal length F, the following parameters are defined,

$$x = \frac{X}{F},\ y = \frac{Y}{F},\ n = \frac{N}{F},$$
$$g = \frac{G}{F},\ \text{and}\ w = \frac{W - W_o}{F}.$$

For convenience we will also define

$$a_0 = \cos(\alpha), \quad \text{and} \quad b_0 = \sin(\alpha).$$

Equation (4.1) to (4.3) become

$$\begin{aligned} \frac{\overrightarrow{F_1P}}{F} &= 1 - w - b_0 n, & (4.7)\\ \frac{\overrightarrow{F_2P}}{F} &= 1 - w + b_0 n, \end{aligned}$$

and

$$\frac{\overrightarrow{F_0P}}{F} = g + w. \tag{4.8}$$

Equation (4.4) to (4.6) become

$$\begin{aligned} \frac{(\overrightarrow{F_1P})^2}{F^2} &= 1 + y^2 + x^2 - 2a_0y - 2b_0x, \\ \frac{(\overrightarrow{F_2P})^2}{F^2} &= 1 + y^2 + x^2 - 2a_0y + 2b_0x, \end{aligned} \tag{4.9}$$

and

$$\frac{(\overrightarrow{F_0P})^2}{F^2} = (g - y)^2 + x^2.$$

By combining the normalised forms of Equations (4.7) and (4.9),

$$\begin{aligned} (1 - w - b_0n)^2 &= 1 + y^2 + x^2 - 2a_0y - 2b_0x, \\ 1 + w^2 + b_0^2n^2 - 2b_0wn - 2w &= 1 + y^2 + x^2 - 2a_0y - 2b_0x. \end{aligned} \tag{4.10}$$

Since the off axis focal points are located symmetrically about he centre axis, the lens contours must also be symmetrical. Therefore, Equation (4.10) remains unchanged and can be separated into two independent equations if x is replaced by $-x$ and n by $-n$. One equation contains only odd powers of x and n while the other contains the even terms. Therefore,

$$\begin{aligned} -2b_0n + 2b_0wn &= -2b_0x, \\ x &= n(1 - w), \end{aligned} \tag{4.11}$$

and

$$y^2 + x^2 - 2a_0y = w^2 + b_0^2n^2 - 2w. \tag{4.12}$$

Equations (4.6) and (4.8) may be combined in the same way resulting in

$$\frac{\overrightarrow{F_0P}^2}{F^2} = (g - w)^2 = (g - y)^2 + x^2,$$

and

$$y^2 + x^2 - 2gy = w^2 - 2gw. \tag{4.13}$$

By subtracting Equations (4.12) and (4.13), the following relation is derived,

$$y = \frac{b_0^2n^2 + 2w(g - 1)}{2(g - a_0)}, \tag{4.14}$$

Equations (4.11) and (4.14) are substituted into Equation (4.12) and the resultant quadratic equation is solved to find w. The quadratic equation is

$$Aw^2 + Bw + C = 0, \tag{4.15}$$

where

$$A = 1 - \frac{(g-1)^2}{(g-a_0)^2} - n^2, \tag{4.16}$$

$$B = -2g - n^2 b_0^2 \frac{g-1}{(g-a_0)^2} + 2g\frac{g-1}{g-a_0} + 2n^2, \tag{4.17}$$

$$C = -\frac{n^4 b_0^4}{4(g-a_0)^2} + g\frac{n^2 b_0^2}{g-a_0} - n^2. \tag{4.18}$$

By noting that the lens arc must pass through the origin, the value of w can be calculated using the formulae

$$w = \frac{-B - \sqrt{B^2 - 4AC}}{2A} \ (g \geq a_0),$$

$$w = \frac{-B + \sqrt{B^2 - 4AC}}{2A} \ (g < a_0).$$

These equations have been further simplified (Katagi et al. 1982, Katagi et al. 1984) by showing that

$$B^2 - 4AC = \frac{b_0^4}{(g-a_0)^2}\left(1 - n^2\right)\left(n_1^2 - n^2\right)\left(n_2^2 - n^2\right),$$

where

$$n_{12}^2 = 2\frac{g(1-a_0) + (g-1)^2 \pm (g-1)\sqrt{(g-a_0)^2 + b_0^2}}{b_0^2}.$$

For the Rotman equations to yield real values for x and y, $B^2 - 4AC \geq 0$. This leads to the result that $0 \leq |n| \leq \min(1, n_1, n_2)$.

Once the design parameters α and g are chosen, w can be computed as a function of n from Equation (4.15). These values are substituted into Equations (4.10) and (4.11) to determine x and y.

Beam Port Positions and Delays

The work of Rotman and Turner (1963) suggests that the beam ports should be positioned on the focal arc at the desired beam pointing angle θ from the axis. The radius of the focal arc is calculated using the equation

$$R = \frac{(Fa - G)^2 + F^2 b^2}{2(G - Fa)}. \tag{4.19}$$

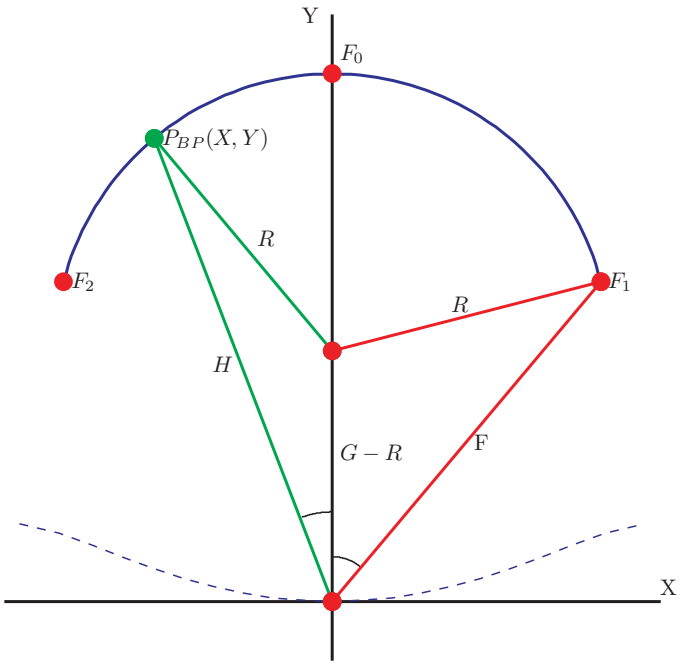

Figure 4.3: Focal arc geometry. The Rotman equations do not define the shape of the focal arc connecting the three perfect focal points. The focal arc is normally chosen to be a circle connecting all three points. This figure shows the focal arc, $P_{BP}(X,Y)$, with radius R, centred on the point $G-R$ from the origin. If multiple beam ports are fed together with a common array phase centre, the additional delay lines must be added to each beam port of $G-H$.

The beam ports are placed at an angle θ from the axis and length H from the origin as shown in Figure 4.3. The length H is found using the trigonometric law of cosines, from the triangle with sides R, H, and $G-R$. The equation is

$$H = \frac{-B_f + \sqrt{B_f^2 - 4A_fC_f}}{2A_f}, \tag{4.20}$$

where

$$\begin{aligned} A_f &= 1, \\ B_f &= -2(G-R)\cos(\theta), \\ C_f &= G^2 - 2RG. \end{aligned}$$

The coordinates of the beam port, $P_{BP}(X, Y)$, are then found using

$$\begin{aligned} X_f &= H\sin(\theta), \\ Y_f &= H\cos(\theta). \end{aligned}$$

Applications involving beam synthesis, achieved using combinations of beams, require that all beams must have the same far-field phase reference. This is achieved by adding delay lines to each beam port so that the path length from any input port to the origin of the lens is constant. The beam port delay line length is calculated using the formula

$$W_f = G - H.$$

4.2.2 Effect of Parameters and Lens Shape

The Rotman lens geometry provides five parameters that are varied in order to achieve optimal lens design. These parameters are α, β, f, g and $n_{\max}$. The parameter $n_{\max}$ is defined by the size of the desired aperture. The remaining variables are optimised to ensure that the lens is realisable and the performance is maximised.

Effect of g

The parameter g changes the distance of the central focal point from the origin of the lens. The factor g determines the extent of the focal arc curvature. Figure 4.4(a) shows that increasing g results in stronger curvature of the focal arc and reducing the curvature of the lens contour. When selecting the value of g, the primary goal is the minimisation of path length errors for all points on the focal arc.

The Rotman equations result in a lens with three perfect focal points at F_0, F_1 and F_2. The equations do not specify an optimum value of g that minimises the path length aberrations on the focal arc between these points. Rotman uses the phase error analysis of the Ruze lens to suggest an optimum value of

$$g = 1 + \frac{\alpha^2}{2}. \tag{4.21}$$

Rotman and Turner (1963) demonstrated numerically that path length errors of less than $\pm 0.0001F$ can be achieved for a field-of-view of $\pm$ 35° using $|n| \leq 0.53$, $\alpha = 30°$, and g calculated with Equation (4.21). Ruze (1950) demonstrated that his lens is capable of

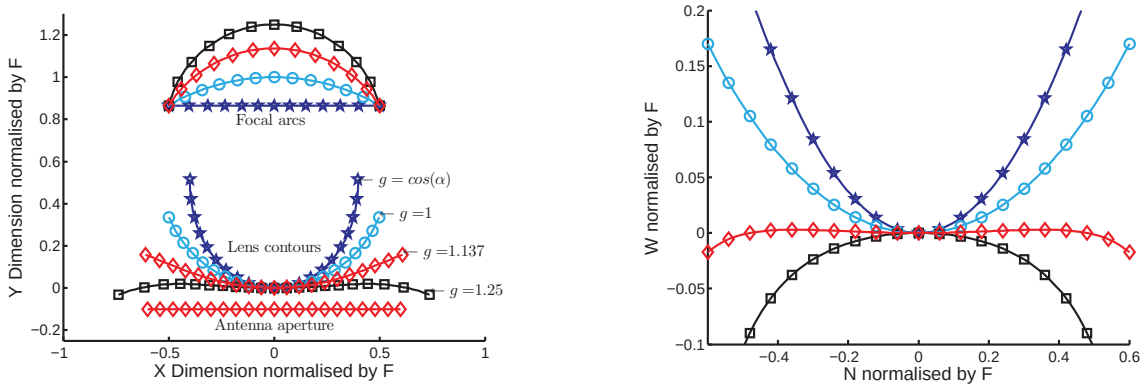

(a) Normalised lens contour curves.

(b) Normalised delay line lengths.

Fig. 4.4: Effect of parameter g. The parameter g defines the distance of the central focal point from the origin. Subfigure (a) shows the effect of varying g on the lens contour and Subfigure (b) shows the effect on the delay line lengths of the Rotman lens. The parameters used to generate these figures are $g = 0.866, 1, 1.137, 1.25$, $\alpha = 30°$, and $n_{\text{max}} = 0.6$. Both lens contour curves and delay line lengths are normalised by the focal length F.

scanning one-degree beams over angles as great as 100 beamwidths. Rotman and Turner (1963) used similar arguments to show the their lens can be used to scan 0.1 degree beams over 800 beamwidths.

A geometrical optics error analysis of a number of constrained lenses (Smith 1982) suggests that the optimal g is given by,

$$g = 1/\cos(\alpha). \tag{4.22}$$

Smith (1982) concludes that this will result in aberrations of the same magnitude (6×10^{-4}) but higher order than that of $g = 1$. No comparison was made to the value for g suggested by Rotman in Equation (4.21).

Little work has been carried out to test the values of g suggested by Rotman and Turner (1963) and Smith (1982). Further, an effective method to find the optimal value of g for any value of α and f would be an important contribution to the design of wide aperture lenses. This will be discussed further in Section 5.2.

Effect of α

The angle between the outer focal points and the origin is defined by α. The variable α is generally considered to define the field-of-view of the Rotman lens because aberrations

increase rapidly for beam angles greater than α. For this reason, the selection of α is limited by the scanning requirements of the lens and the maximum acceptable error. Figure 4.5(a) shows that as α is increased the width of the lens is increased. The choice of α also strongly varies the lens contour and the delay line length.

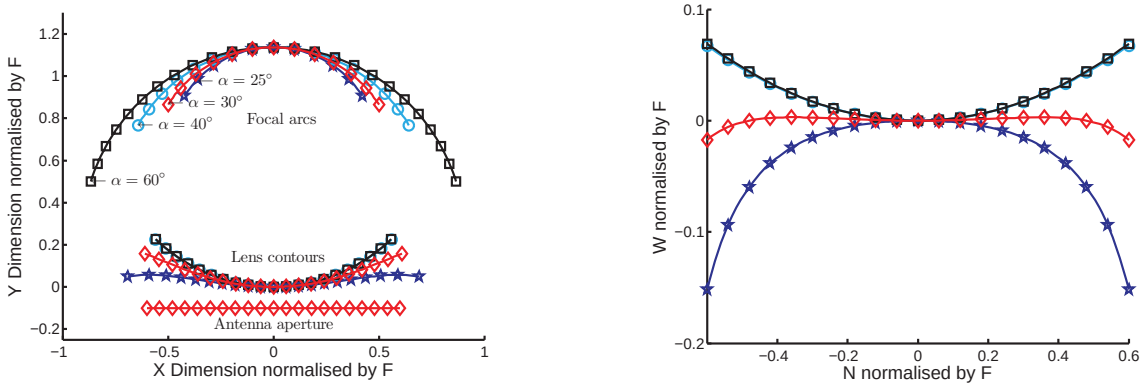

(a) Normalised lens contour curves.

(b) Normalised delay line lengths.

Fig. 4.5: Effect of parameter α. The parameter α defines the angle between the central focal point and the outer focal points when viewed from the origin of the lens. This is generally set to be equal to the maximum scan angle of the lens. The parameters used to generate these figures are $\alpha = 25°$, $30°$, $40°$, $60°$, $n_{\text{max}} = 0.6$, and $g = 1.137$. Both lens contours and delay line lengths are normalised by focal length F.

Effect of n

The position of the antenna element on the aperture and its associated port on the antenna arc of the Rotman lens is defined by n. The largest value, n_{max}, dictates the portion of the total antenna arc used by the lens. Larger values of n_{max} produce impractical antenna arc shape as seen in Figure 4.6(a). Moreover, Figure 4.6(b) shows that the increased length of the outer delay lines make the lens difficult to implement for larger n_{max}.

The parameter n_{max} varies the size of the antenna aperture because the lens dimensions have been normalised by the focal length F. After the lens is designed it must be scaled to match the antenna aperture. The error analysis and lens design are simplified by normalising the lens by the aperture size. The effect of varying the antenna element spacing relative to the antenna port spacing has also been neglected in this analysis. These points will be discussed further in Section 5.1.

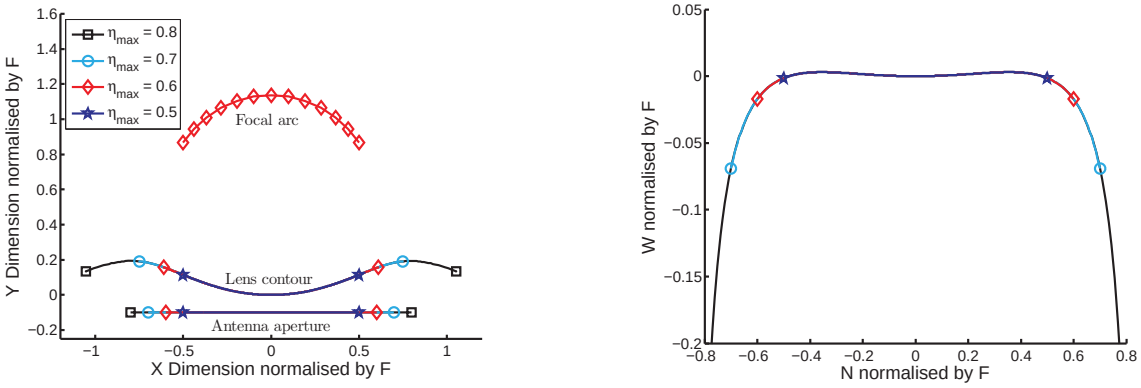

(a) Normalised lens contour curves.

(b) Normalised delay line lengths.

Fig. 4.6: Effect of parameter n_{max}. The size of the array aperture, and therefore the size of the lens contour, is defined by the parameter n_{max}. This variable has no effect on the three focal points or the delay line length. The parameters used to generate these figures are $n_{\text{max}} = 0.5, 0.6, 0.7, 0.8$, $\alpha = 30°$, and $g = 1.137$. Both lens contour curves and delay line lengths are normalised by focal length F.

4.2.3 Alternate Focal Arcs

The Rotman lens equations define a lens contour based on the positions of three perfect focal points, one on the axis and two symmetrically either side. The focal arc passing through these three focal points is not defined by the Rotman equations, however it is commonly implemented using a circular geometry. Although other focal arcs have been demonstrated in the literature, no systematic analysis of the problem has been carried out. The following sections will describe the alternatives to the circular focal arc.

Parabolic, Hyperbolic, Elliptical & Straight Focal Arcs

Parabolic, hyperbolic, elliptical and straight focal arcs have been compared in the literature (Singhal et al. 1998). Singhal et al. (1998) concluded that a more compact Rotman lens is obtainable using an elliptical focal arc while maintaining comparable aberrations. The analysis is based on the results of contour integral simulations where the beam ports are implemented as tapered transmission lines connected to the body of the lens. The contour integral simulation includes the effects of port mismatch and reflections within the body of the lens. The path length errors associated with the Rotman lens are very small compared to the phase errors introduced by these effects. Although the results

described by Singhal et al. (1998) are valid for a single lens implementation, they do not provide any insight into the optimal focal arc for the Rotman lens.

Symmetric Rotman Lens

Equations describing a symmetric Rotman lens that produces lens and feed curves identical with opposite orientations have been presented in the literature (Shelton 1978). The port locations and delay at each point on the lens and feed curves are also identical. The resulting lens exhibits front-back and right-left symmetry. This makes it possible to interchange the input ports and array ports.

Shelton (1978) suggests six reasons for choosing the symmetric configuration over the asymmetric lens:

1. asymmetric lenses have the lens arc or feed arc more strongly curved than the arcs obtained for the symmetric solution;
2. symmetric lenses exhibit better aberration characteristics;
3. the self-illumination problem—the tendency for feed ports to illuminate other feed ports, is more severe for asymmetric lenses;
4. the symmetric lens is smaller than an equivalent asymmetric lens;
5. it is possible to divide a symmetric lens on its line of symmetry with a reflecting plane and realise a reflection-type collimating system; and
6. beam synthesis, such as the formation of monopulse patterns using combinations of beams, can only be achieved using the symmetric configuration.

Shelton (1978) states that the first four items are not rigorously proven. This will be addressed in Section 5.3.1. Shelton (1978) presented design equations that demonstrate that these symmetrically configured lenses form a one-parameter family. The design equations are not simply an extension of the Rotman equations, defining g, α and n, instead they define the lens in terms of A and C, shown in Figure 4.7. From A and C, the lens contours are defined and the lens dimensions are then scaled so that the lens has transmission characteristics equivalent to those of a Butler matrix with the same number of ports.

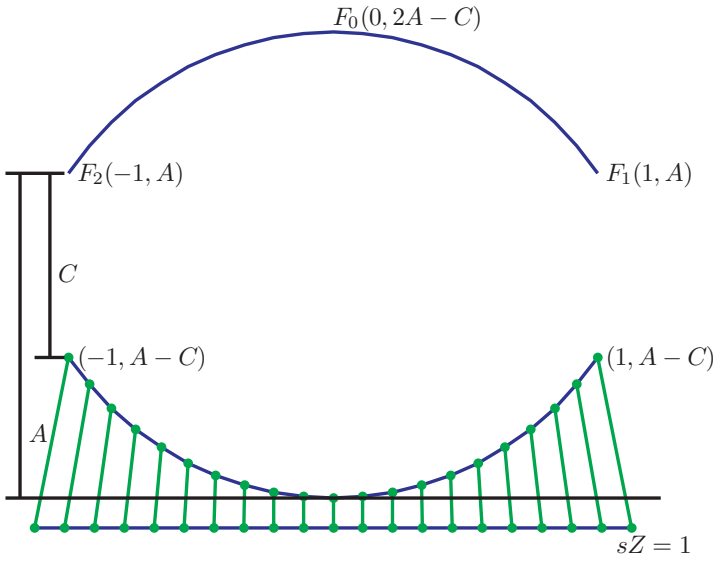

Figure 4.7: Symmetrical Rotman lens geometry. The symmetrical Rotman lens replaces the circular focal arc with the array arc. The resultant lens is symmetrical and therefore beam ports and antenna ports are interchangeable. The symmetrical lens is very different from that of Rotman and Turner (1963). Instead of defining the lens based on F, G, and α, the symmetrical lens uses the variables A and C shown above.

A set of equations relating the asymmetric Rotman lens variables, g, α and n to the symmetric variables A and C, has not been defined; further, a comparison of the performance of the symmetrical and asymmetrical lens, and confirmation of Shelton's six points, have not been presented in the literature.

Refocusing

There are many examples in the literature regarding the refocusing of single and dual focal point lenses to improve the lens aberration performance (Kock 1946, Ruze 1950). Similar effort has not been applied to the Rotman lens architecture. This may be due to the significant performance improvement of the Rotman lens in comparison to single and dual focal point lenses. Refocusing is a problem space that warrants closer attention.

4.3 Electromagnetic Models

4.3.1 Two Dimensional Aperture Model

The analysis of the Rotman lens so far, has concentrated on the path length performance, but has not considered the amplitude performance. To improve the accuracy of the lens model, a number of attempts have been made to predict the coupling coefficients between any two ports (Maybell 1981, Tomasic and Hessel 1982). Smith and Fong (1983) approximated the waveguide ports as two-dimensional antennas with a cosine aperture field distribution, and uniform aperture field distribution to approximate a microstrip or stripline port (Smith and Fong 1984). This approach predicts the primary amplitude distribution across the array ports of the lens allowing predictions of insertion loss and sidelobe levels of the lens fed array.

This model treats the lens ports as two-dimensional antennas as shown in Figure 4.8. The coupling between all ports on the lens is calculated using the two-dimensional equivalent of the Friis transmission equation. From this, approximate values for insertion loss and excitation taper across the antenna elements can be determined.

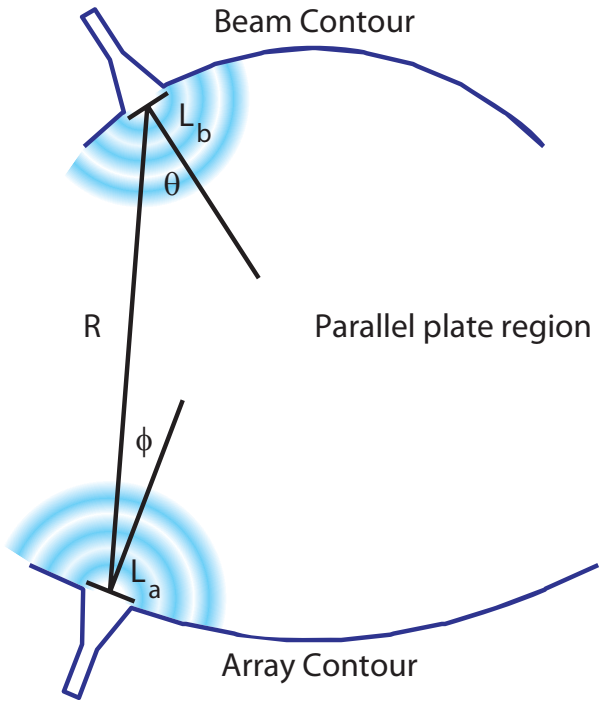

Figure 4.8: Two dimensional aperture model. Beam port and antenna port of the lens represented as two-dimensional transmitting and receiving antennas. This allows predictions of port coupling, lens insertion loss, and sidelobe levels.

We first define the two-dimensional antenna gain $G(\theta)$ by

$$S_d = \frac{P_t}{2\pi r h},$$

where S_d = power flux density, P_t = power transmitted, r = distance away from the antenna, and h is the parallel plate separation.

The maximum gain of a uniformly illuminated aperture of width L is

$$G_{\max} = \frac{2\pi L}{\lambda},$$

compared to

$$G_{\max} = \frac{4\pi A}{\lambda^2},$$

for the three dimensional case (Smith and Fong 1984).

The two-dimensional equivalent of the Friss transmission formula can now be derived:

$$\begin{aligned} P_r &= S_d(\theta) A_r(\phi) \\ &= \frac{P_t G(\theta)}{2\pi r h} L_e(\phi) h, \end{aligned}$$

and

$$\frac{P_r}{P_t} = \frac{\lambda}{4\pi^2 r} G_t(\theta) G_r(\phi),$$

where θ and ϕ are angles from the normals to the beam and array port apertures. As expected this closely resembles the three dimensional case

$$\frac{P_r}{P_t} = \frac{\lambda^2}{(4\pi)^2 r^2} G_t G_r.$$

The function $G(\theta)$, describing the radiation pattern for a flared microstrip port, is found using two dimensional aperture theory (Clarke and Brown 1980). The junction between the flared microstrip line and the parallel plate region of the lens is approximated as a uniform aperture field distribution across the width l of the microstrip line or stripline (Fong and Smith 1984). This leads to the following formula

$$G(\theta) = \frac{2\pi l}{\lambda} \{ \frac{\sin(\frac{\pi l \sin\theta}{\lambda})}{\frac{\pi l \sin\theta}{\lambda}} \}^2 \cos^2\theta.$$

When using waveguide feed horns we assume a half cosine aperture distribution (Smith and Fong 1983), this yields

$$G(\theta) = \frac{2\pi l}{\lambda} \frac{8}{\pi^2} \{ \frac{\cos(\frac{\pi l \sin\theta}{\lambda})}{1 - (\frac{2 l \sin\theta}{\lambda})^2} \}^2 \cos^2\theta.$$

The two dimensional aperture model is a valuable visualisation tool providing a quick and intuitive method of exploring the phase and magnitude performance of different Rotman lens geometries. However, the two dimensional aperture model assumes that all ports are perfectly matched to lossless transmission lines. This model does not predict reflections and scattering within the body of the lens.

4.3.2 Planar Electromagnetic Models

The geometrical optics and two dimensional aperture models yield only an approximate design because the effect of port reflections, mutual coupling, and scattering between ports is not included. A number of attempts have been made to combat this with limited success (Richards et al. 1987, Tripp et al. 1989, Shishegar and Safavi Naeini 1996, Penney et al. 2005, Silvestro et al. 2005, Schulwitz and Mortazawi 2006). The models based on planar circuit analysis have proved effective. For the first time, internal lens reflections and mutual coupling between ports could be accurately predicted. Planar circuit analysis assumes that the electric and magnetic fields within microstrip or stripline devices are invariant across the depth of the substrate. This permits these devices to be modelled as two-dimensional structures.

Early work involving microstrip and stripline transverse electromagnetic (TEM) lenses introduced two-dimensional integral equations relating the electric and magnetic fields along the periphery of the lens (Chan 1989a, Sharma et al. 1992). Chan's (1989b) approach offered the improvement of using waveguide-like modes in the lens feeds, enhancing the efficiency of analysis. This approach has been used extensively in the design of microstrip and stripline Rotman lenses (Yuan and Liang 1999, Yuan et al. 1999). A similar approach was adapted by the authors in the design of lenses using rectangular waveguide at millimetre-wave frequencies (Peterson and Rausch 1999b, Peterson and Rausch 1999a).

Recent work (Yuan et al. 2001) improves the accuracy of the analysis significantly, based on a hybrid procedure that combines the least squares finite element method (LSFEM) (Wendland 1979) and the transfinite element method (Cendes and Lee 1988), which is appropriate for any planar beam-forming lens structure. In contrast to earlier methods, the LSFEM method solves the full first-order Maxwell system by incorporating the two divergence equations explicitly in the functional, and has been shown to be free from spurious solutions even when standard nodal finite elements are used (Jiang 1998).

To demonstrate that the method produces accurate results, Chan (1989a) applied the method to the analysis of a multiple beam-forming Rotman lens. The results begin to converge when the area of each element becomes smaller than approximately $\lambda/50$. Yuan et al. (2001) state that accurate results are obtained when the element area is reduced to $\lambda^2/150$. The procedure yields the distribution of the electromagnetic fields in the lens, as well as the scattering parameters.

While significant work has been carried out in the literature on the design of efficient solvers capable of calculating the performance of a Rotman lens, there are many commercial electromagnetic simulation packages available that are capable of this task (Penney 2008). The open boundary methods of moments solver, such as Ansoft Designer (Ansoft 2008a), is particularly well suited, since it is capable of accurately representing angled ports and edges.

4.3.3 Monolithic Port Design

Port design, after beam port position is determined, is the second stage of lens design and it will be shown in Section 7.1 that port design is the most challenging aspect of monolithic constrained lens implementation. Before electromagnetic simulation techniques became available, port design was reliant on measured results of realised structures. While this approach worked very well for E-plane probe port designs, the physical structure of microstrip and stripline ports is not easily tuned. Electromagnetic analysis has made it practical to tune the virtual structures and confidently predict the effects on a constrained lens design. It is for these reasons that little work was carried out in this area before (1989a).

The port connects the microstrip or stripline to the parallel plate region of the lens providing a transformation between the two. Poorly designed ports result in beam pattern degradation due to internal reflections and increased return loss. The problem is exacerbated by the need for electromagnetic simulation or construction of a prototype to measure the performance of a given port implementation. This thesis is significant in that it explores port design independent of lens implementation, which is necessary if broadband Rotman lenses are to emerge.

Tapered port

Early lens designs used flared waveguide to implement the beam ports. Early monolithic lens designs used the same approach. Unlike the impedance tapers described in Section 3.3.4, the characteristic impedance at each point on the taper is not known. This approach gently flares the microstrip or stripline to half the guided wavelength where it attaches to the body of the lens (Niazi 1980, Maybell 1981, Niazi 1981, Herd and Pozar 1984). The layout of this port design is shown in Figure 4.9. By gradually increasing the width of the transmission line the characteristic impedance is slowly changed to resemble the impedance at the interface between the port and lens body. Reducing the port angle reduces the discontinuity in the impedance taper and results in an improved match (Musa and Smith 1986). Experimental results demonstrate that a taper angle of less than 12.5° is required for a good match (Musa and Smith 1989).

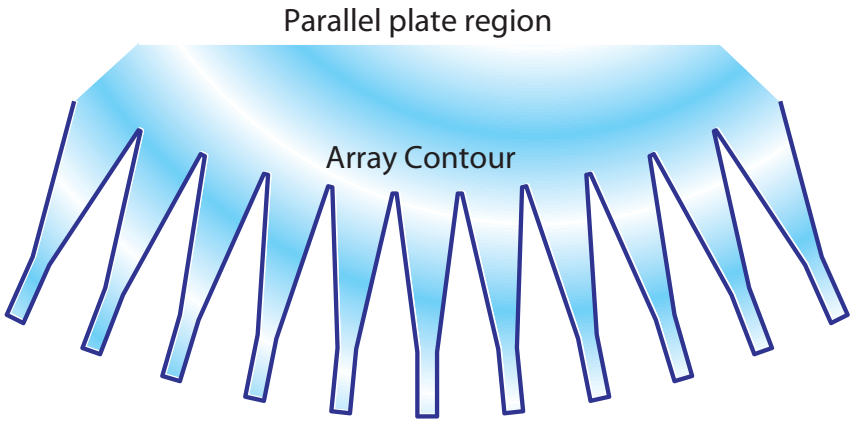

Figure 4.9: Tapered port. Early lens designs use a simple tapered port. The gradual increase in transmission line width acts as a slow impedance taper and improves the impedance match of the port.

Beam ports positioned on the edge of the focal arc do not illuminate the lens contour ideally. Some authors have rotated the beam port in an attempt to direct the energy more favourably. Experimental results showed this to be quite an effective technique (Musa and Smith 1986). Other designers used H-plane sectoral horn antenna data to approximate the position of the port phase centre relative to the port mouth (Herd and Pozar 1984). By placing the beam ports in front of the focal arc by a small margin, the phase centre of the port is exactly on the focal arc and phase errors are reduced.

Port Impedance Matching

The impedance matched port is used in an attempt to directly match the impedance at the periphery of the lens body to the transmission line using a series impedance transformer (Chan et al. 1990b, Chan et al. 1990a, Chan et al. 1994, Chan and Rao 2002, Chio and Chan 2004, Maybell et al. 2005), using techniques described in Section 3.3.3. The challenge with this approach is finding the required impedance of each port. Chan (1989a) uses boundary integral equation method to generate the S-matrix representing the lens body (Chan 1989b). The reflection coefficient of each port is converted to an impedance and this value is assumed to achieve a perfect match. By repeating this at a number of frequencies a broadband port impedance is defined that provides sufficient information for the multi stage quarter wavelength series impedance transformer, as seen in Figure 4.10, to be designed.

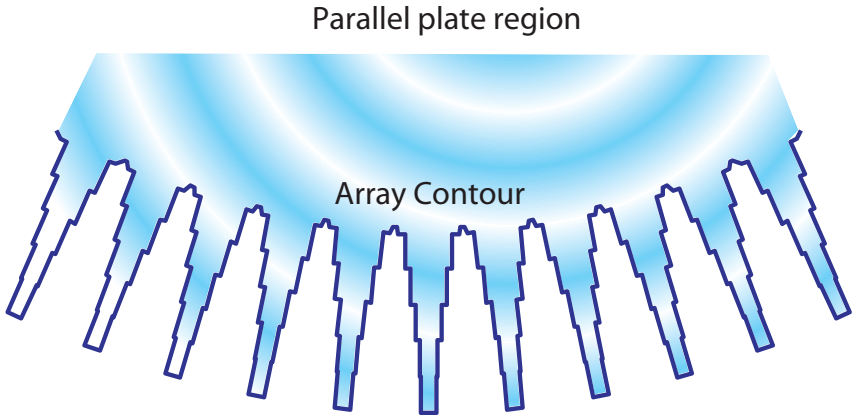

Figure 4.10: Impedance matched port design. If the port impedance is known, a multi-segment impedance matching network can be used to implement a broadband match. This technique allows the impedance the port presents to the body of the lens to be defined precisely.

This matching method is appropriate for matching ports of the Rotman lens that are excited only when no other port is excited. An example is shown in Figure 4.11 where only a single beam port is being excited. The matching method begins by examining the lens power-wave S-parameters, described in Section 3.2.4. The input impedance of the port of interest, port i, is calculated using the formula:

$$\mathbf{Z}_{\text{in},i} = \Re(\mathbf{Z}_{\text{ref},i})\Re(z) + j(\Re(\mathbf{Z}_{\text{ref},i})\Im(z) - \Im(\mathbf{Z}_{\text{ref},i}))$$

where

$$z = \frac{1+\mathbf{S}_{ii}}{1-\mathbf{S}_{ii}}.$$

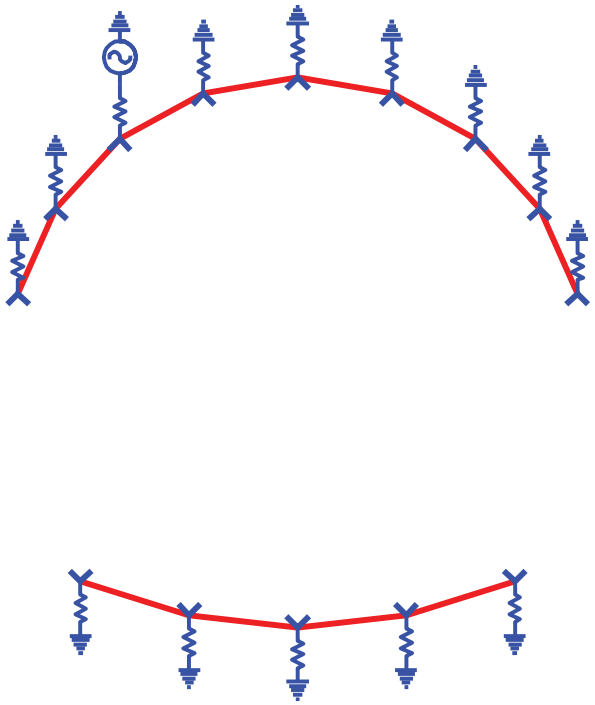

Figure 4.11: Beam port matching. Beam ports are treated as if they are the only driven port in the system. The input impedance is calculated from the reflected power-wave at port i which is equal to $\mathbf{S_{ii}}$. By repeating this process for each beam port, an effective match is achieved across all beam ports.

The S-parameters are recalculated using new reference impedances. By setting

$$\mathbf{Z}'_{\text{ref}} = \mathbf{Z}_S,$$

$\mathbf{S}'$ is calculated using Equations (3.10) and (3.12) and represents the behaviour of the system with the new source impedances. By setting the source impedance $\mathbf{Z}_{\text{s},i}$, of port i, equal to the conjugate of the input impedance $\mathbf{Z}_{\text{in},i}$ a perfect match for port i is achieved. To match all beam ports of the lens, this procedure must be repeated for each beam port. However, changing the source impedance of any beam port alters the input impedance of all others. For this reason, none of the beam ports are perfectly matched and the process must be repeated until all individually excited ports are effectively matched.

The problem with this approach is that the impedance experienced at each port is dependent on the terminated impedance of all other ports. Despite each port being individually matched, the process described by Chan et al. (1994) does not achieve a match when multiple ports are excited simultaneously. A significant contribution of this thesis is that it will establish a procedure that correctly accounts for multiple port excitation while effectively matching all ports of a constrained lens.

Sidelobe Reduction

The width of monolithic ports is limited to $\lambda/2$ to prevent coupling to second order modes. As the width of the beam port increases, its two dimensional beam pattern becomes narrower. This causes excitation taper across the antenna array that resembles a cosine taper. The cosine taper exhibits lower sidelobes than the uniformly excited array aperture (Musa and Smith 1986, Musa and Smith 1989). An example of this is seen in Figure 4.12(a). The main beam width is increased while the sidelobes are reduced Figure 4.12(b). The excitation taper also results in a greater proportion of the energy coupling with the antenna ports, decreasing the insertion loss. To achieve a cosine taper, the beam port must be made larger than half a wavelength by feeding two or more adjacent ports.

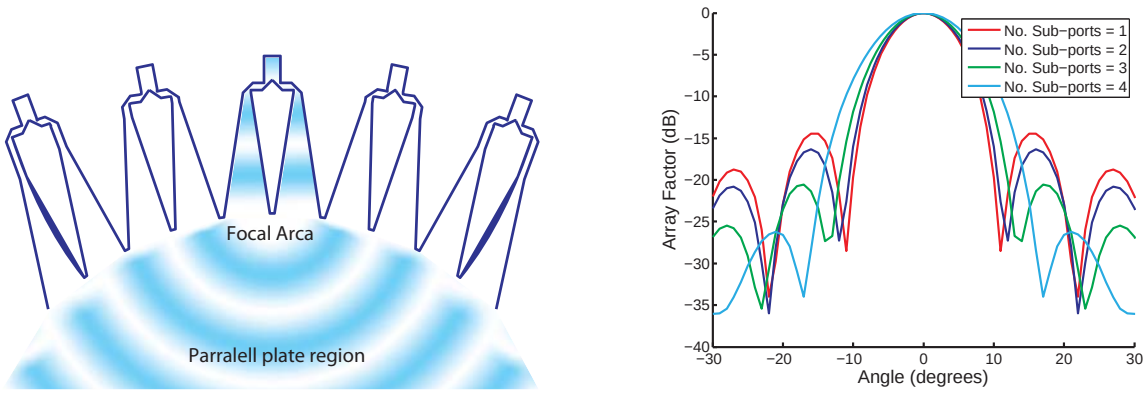

(a) Multi-port implementation.

(b) Beam pattern.

Fig. 4.12: Multi-port beam port implementation. Constructing a beam port by combining two adjacent ports together using a power divider or combiner results in a more directional beam pattern. This helps prevent second order modes and reduces the energy lost to the sidewall of the lens. The coupling between each sub-port must be considered to achieve a good match. Subfigure (a) demonstrates a focal arc consisting of linear tapered sub-ports connected in pairs to form beam ports. Subfigure (b) demonstrates the increase in directivity of the port as the number of sub-ports is increased.

A number of authors have reduced the sidelobe performance of the lens by combining three to five beam ports to implement a Taylor series approximation (Thomas 1978, Tomasic and Hessel 1982, Troychak 1987, Peterson and Rausch 1999b). Thomas (1978) showed that a 8th order Taylor series beam port excitation, designed to achieve -45 dB sidelobes, could be approximated by three ports and still achieve -43 dB sidelobes. Experimental

results showed that sidelobes were increased further to -29.9 dB, for a 10 % bandwidth at 6 GHz, due to phase errors in the antenna feed lines.

The effect of feeding multiple beam ports is that the cross over points between adjacent beams become unacceptably low for most applications. To counter this, complex feed networks must be implemented to allow beam ports to be connected to multiple feeds. Smith (1985) suggested using Wilkinson dividers back to back to implement N feeds, utilising $N + 1$ beam ports, as seen in Figure 4.13(a). This results in each beam port being fed while maintaining closely spaced beams at the cost of 3 dB insertion loss. The loss occurs in the resistive terminations of the two way hybrid junctions connected to each beam port.

Other feed networks have been suggested for feeding triple sub-port systems. Figure 4.13(b) uses two and three way hybrid power splitters to implement 0.7:1:0.7 amplitude excitation. This power splitting network results in 1.76 dB insertion loss. A 0.5:1:0.5 amplitude excitation taper is generated by the power dividing network shown in Figure 4.13(c). This network is simple to implement in microstrip as it uses only two way hybrids. This network has a 1.25 dB insertion loss (Smith 1985). Despite the potential benefits, the insertion loss, cost, and complexity has prevented more than passing interest in these feed networks.

4.3.4 Dummy ports and sidewalls

It has become standard practice in waveguide based lens design, to reduce the reflections from the sidewalls of the lens by replacing the air dielectric with Radiation Absorbing Material (RAM). This is not practical for monolithic lens designs, instead dummy ports terminated in a matched load are positioned along the lens sidewall (Niazi 1980, Fong and Smith 1984, Musa and Smith 1989). Chan et al. (1994) connected the dummy ports to lossy microstrip lines resulting in significant cost and size reduction.

Like beam and antenna ports, dummy ports exhibit a directional two dimensional beam pattern. This results in much of the energy incident on the ports from oblique angles to be reflected back into the body of the lens. These effects combined with the material cost and substantial design effort has motivated other sidewall designs. The sidewalls of the lens shown in Figure 4.14, (dubbed *batman*), trap and dissipate energy that would otherwise be reflected back into the body of the lens (Abbott and Parfitt 1997). Other

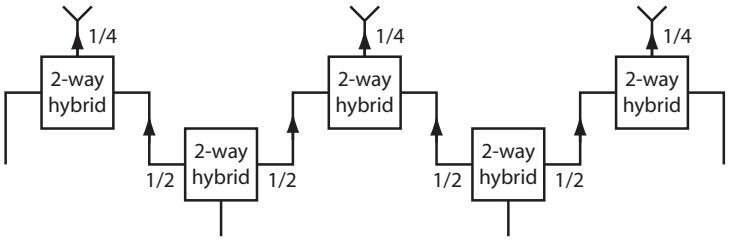

(a) Overlapped dual-port feed.

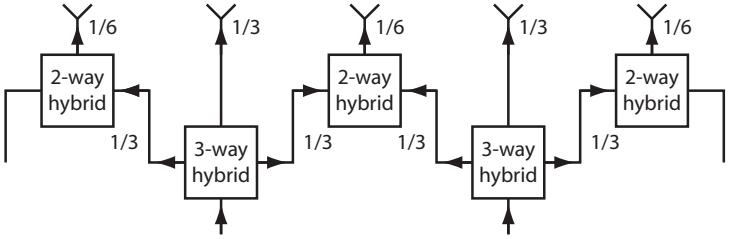

(b) Tri-port feed 1.

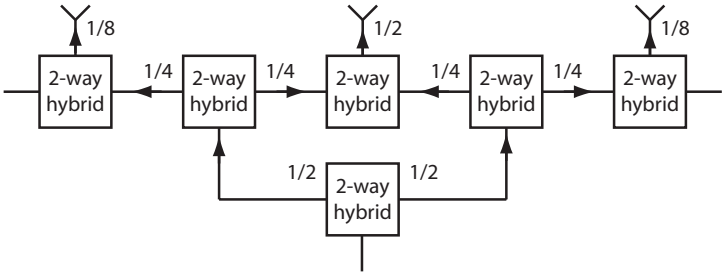

(c) Tri-port feed 2.

Fig. 4.13: Multi-port feed networks. Three methods of implementing overlapped sub-port feeds is shown here. Subfigure (a) uses a linear excitation taper feeding two sub-ports and has a 3 dB insertion loss. Subfigures (b) and (c) feed three sub-ports using a tapered excitation. The feed shown in Subfigure (b) has an insertion loss of 1.76 dB while the feed in Subfigure (b) achieves 1.25 dB.

authors use resistive foil placed over the sidewalls to reduce the strength of the reflected energy (Metz et al. 2001a).

Figure 4.14: Batman sidewall. Attempts to reduce design effort and complexity of sidewall absorbers and dummy ports motivated some interesting designs. The above *batman* design was reported by Abbott and Parfitt (1997).

The poor performance of dummy ports or sidewall absorbing material can significantly limit the performance of Rotman lens architectures.

4.4 Rotman lens designs in the literature

The Rotman lens has been implemented using a large range of transmission lines and antenna elements. These lenses have been built to operate from microwave frequencies to near visible light. Despite the apparent simplicity of the Rotman lens concept, the implementation of these devices provides many challenges. To better understand these challenges, this section provides a summary of constrained lens designs presented in the literature.

4.4.1 E-plane Probe and Waveguide Horn

Despite the simplicity of reflector backed E-plane probes, used to implement the ports of the first Rotman lens (Rotman and Turner 1963), the literature does not report any new

lenses built until the work carried out by Thomas (1978) on reducing sidelobe levels of multi-beam arrays and the construction of wide angle array feeds (Thomas 1978). The E-plane probe feed structure was examined in detail by Tomasic and Hessel (1982) with the intention of reducing the lens sidelobe levels and improving matching. The Rotman lens has also been used as the transform feed for a 9 GHz dual lens Fourier transform antenna array (Thomas 1979, Southall and McGrath 1986). A detailed explanation of the completely overlapped sub-array antenna is beyond the scope of this thesis. However, Southall and McGrath (1986) utilised dummy ports to significantly improve the illumination of the antenna ports by the outermost beam ports.

4.4.2 Waveguide

The quest for ever higher frequencies and reduced insertion loss motivated the construction of Rotman lenses using waveguide (Rausch and Peterson 1992). These designs operate at 37 GHz, have 32 array elements, 17 beams and a maximum scan angle of 22.2°. These lenses are realised in aluminum using electrical discharge machining techniques. The lens is fed using WR22 rectangular waveguide, with a folded magic-T used to split each feed into two ports to eliminate the possibility of higher order waveguide modes. The regions along the sidewall are specially shaped and lined with absorber material to eliminate reflections within the body of the lens.

The electromagnetic model used to design these lenses is similar to that proposed by Chan (1989a). This model was used to optimise the port widths and predict the side lobe level and insertion loss (Peterson and Rausch 1999b, Peterson and Rausch 1999b).

Rausch et al. (1996) highlighted the importance of sidewall design and maximum port width. Beam patterns were calculated after applying a 3rd order Taylor series excitation taper designed to achieve sidelobes of -45 dB, compared to -15 dB without the taper (Rausch 1998), and -21 dB by exciting two adjacent phase equalised beam ports (Wiebach and Rausch 1998). Experiment showed a greater than 15 dB increase in sidelobes due to reflections from the sidewalls of the lens when straight sidewalls are used and absorbing material is removed. A similar result is seen when ports widths are increased beyond half a wavelength due to excitation of higher order modes in the ports. Over the frequency range 32.8 GHz to 36.8 GHz the insertion loss ranges from 0.8 dB to 2.3 dB with an increase in insertion loss of 2 dB, due to the Taylor series taper. Typical port isolation is said to be -21 dB at 33 GHz reducing to -28 dB at 37 GHz (Rausch et al. 1997a, Rausch et al. 1997b).

This design approach has been repeated in other papers (Phuong et al. 1999, Kilic and Dahlstrom 2005, Weiss et al. 2002, Weiss and Dahlstrom 2006).

The highest frequency Rotman lens to date is designed for 94 GHz (Fuchs and Nussler 1999, Nubler et al. 2007). This lens is built in the same way as those of Rausch and Peterson (1992). The lens consists of 15 beam ports covering a scan range of $\pm$ 23.3° in steps of 3.3° and 10 array ports. Beam ports have been rotated so that they point at the centre of the output arc to reduce asymmetrical illumination of the array ports. When directly connected to a linear antenna array, an average sidelobe level of less than -10 dB has been obtained, closely agreeing with theoretical results.

A new form of waveguide Rotman lens has emerged using *substrate integrated waveguide* (Sbarra et al. 2007, Cheng et al. 2008). This waveguide solution is low cost since it shares the same manufacturing process as microstrip and stripline lens implementations.

4.4.3 Stripline and Microstrip Lens Design

The size of the Rotman lens can be significantly reduced replacing the parallel plate section with conductively clad dielectric. Beam ports and antenna ports have often been implemented using flared microstrip (Niazi 1980, Maybell 1981, Niazi 1981, Herd and Pozar 1984) or stripline (Maybell 1983). Monolithic construction techniques result in low cost, reduced size and simple implementation of surface mount components. This has made monolithic construction the standard form of Rotman lens construction today.

The first monolithic lens designs are very similar to earlier designs in waveguide. The two dimensional aperture models adopted by designers treat each flared microstrip port as the equivalent flared waveguide, except with a uniform aperture field distribution (Fong and Smith 1984). Experiments to determine the effects of different port geometries and the effectiveness of directional ports resulted in significant improvements in performance (Musa and Smith 1986, Musa and Smith 1989).

The Rotman lens has also found applications in satellite communications and broadcast reception at X-band and K-band frequencies (Gans and Amitay 1983, Sang-Gyu et al. 2005). One application uses a circularly polarised, two dimensional, planar array in a polar scanning system. The angular scan is implemented mechanically while the elevation scanning is implemented using a Rotman lens (Maddocks 1988, Maddocks and Smith 1989, Maddocks and Smith 1991). Early designs featured a single moveable beam port,

or 7 fixed beam ports, implemented using flared waveguide and 24 antenna ports. Later designs utilise triplate (stripline) implementation (Maddocks and Smith 1991).

The Rotman lens has been used to improve the performance of satellite communication systems. One such example is base station beam tilting by the Rotman lens rather than by adjusting mechanical brackets on the antenna array (Kim et al. 1998, Kim et al. 2005, Kim and Barnes 2005). The relatively low frequency of these systems requires a high dielectric substrate to minimise the size of the lens. Further, this application requires that the relatively broad beam be steered over a narrow field-of-view by very small increments. Experimental results showed good beam-forming however the close proximity of beam ports had a detrimental effect on port matching and insertion loss.

The work by Chan (1989a) significantly altered the approach researchers took to designing a Rotman lens by applying a boundary integral equation method to the analysis of stripline and microstrip lenses. Prior to this work, a successful lens design had to rely largely on experimental results obtained from testing, an expensive and cumbersome approach (Chan 1989a). Chan (1989a) found that good port match could not be achieved for significant bandwidths using tapered transmission lines alone (Chan et al. 1990b, Chan et al. 1990a).

The new generation of compact, low cost, high frequency Rotman lenses have found applications in a large number of devices. One of these is a sidelobe canceller for radar applications in the frequency band 8.5 GHz to 10 GHz, constructed using a hexagonal array of horn antennas for used for satellite communications (Chan et al. 1994). This two dimensional array is excited by two banks of Rotman lenses connected in series and rotated by 90° (Chan and Rao 1998, Chan 1999, Chan and Rao 2000, Chan and Rao 2002, Archer and Maybell 2005, Chan et al. 2007).

Other applications that have been proposed include wireless communications (Olsen et al. 2007, Anthony 2008), UHF beamformers (Singhal et al. 2007, Lambrecht et al. 2008), automotive radar (Hall et al. 2004), military radar (Archer and Maybell 2005, Schulwitz and Mortazawi 2005, Schulwitz and Mortazawi 2006, Dongkyu et al. 2007, Schulwitz and Mortazawi 2007, Schulwitz and Mortazawi 2008), and insect vision systems (Goodfellow et al. 1998). The Rotman lens has been used for shared aperture applications. Multiple simultaneous beams are able to be transmitted in different directions and at different frequencies (Jangsoo et al. 2007, Jangsoo et al. 2008). To test this, a 48 beam, 59 antenna element Rotman lens, with frequency range of 8 to 18 GHz, has been constructed (Phuong et al. 1999). The antenna elements were implemented using Vivaldi-notch

elements. The measured insertion loss of this device ranges from 6 to 12.5 dB. After implementing a Taylor weighting function, sidelobes <15 dB were reported.

Modern wireless communications require high bit rates and multiple channels. To support higher channel capacity, *space division multiple access* (SDMA) is proposed to increase the signal to interference ratio. Rotman lenses have been proposed as the beam former component for SDMA architecture (Jaeheung and Barnes 2001). Similar systems have been proposed for high capacity, short range, millimetre wave systems (Tao and Delisle 1996, Tao and Delisle 1997). The wide field-of-view required of these systems means that multiple lenses must be implemented to cover the full 360° sector. Again experiment has shown that beam-forming performance is good, however beam isolation, impedance matching, and insertion loss prove difficult (Tao and Delisle 1998).

A novel application for the Rotman lens in automated road toll systems has been suggested (Peik and Heinstadt 1995). Currently each lane requires a five element array. Instead a 12 element multiple beam microstrip array, fed by a Rotman lens, has been built to simultaneously service five lanes.

Antenna systems for automotive intelligent cruise control applications have been proposed (Williams 1992). The system consists of three switching beams providing coverage of own lane and the two neighbouring lanes and a single wide beam transmit antenna. This application requires a narrow field-of-view utilising 3 to 5 narrow beams operating at 77 GHz. The Rotman lens is ideally suited to this application, the major hurdle being the integration of active devices at such a high frequency (Metz et al. 2001a, Metz et al. 2001b, Denisenko et al. 2001, Zelubowski 1994, Schoebel et al. 2005, Sanghyo et al. 2008, Sinjari and Chowdhury 2008a, Sinjari and Chowdhury 2008b). The feasibility of a passive Ka-band collision avoidance sensor has also been explored in the literature. One system combines the Rotman lens with insect vision processing techniques to detect a potential collision between two vehicles (Hall et al. 2001, Hall et al. 2002).

Combining insect vision with the beam staring monolithic Rotman lens attracted significant interest in the literature. Insect vision processing techniques do not attempt to process an image, instead they rely on tracking moving edges. The processing tasks are less hardware-intensive, resulting in a compact low-cost solution (Abbott and Parfitt 1997). Early work targeted the 37 GHz transmission window and later moved to 94 GHz where black body radiation power is higher. Applications for this technology include:

- guidance for aircraft landing systems,

- guidance for unmanned aerial vehicles (Goodfellow et al. 1998),
- port navigation (Goodfellow et al. 1998), and
- collision avoidance for nanosatellite clusters (Goodfellow and Abbott 1999).

4.4.4 Novel lens architectures

Rotman lenses have been realised using air filled parallel plate and microstrip. Parallel plate Rotman lens designs tend to be large, while microstrip designs tend to encounter high conduction loss at millimetre wave frequencies. Conductive and dielectric loss associated with nonradiative dielectric (NRD) guide decreases with frequency, while the loss of microstrip lines increases with frequency. By implementing the 77 GHz Rotman lens using NRD, conductive and dielectric losses can be reduced by 80 % when compared to microstrip (Jae et al. 2001). Note that NRD guide tends to suffer much higher coupling between beam ports compared to microstrip implementation and this must be taken into account during the design of the lens. The NDR cannot easily be combined with standard antenna elements. A gap-coupled unidirectional dielectric radiator suitable for use at 77 GHz has been built (Jae et al. 2002, Jae et al. 2003). Similar designs have been presented in later papers (Kilic and Weiss 2004, Kilic and Dahlstrom 2005, Kim et al. 2005, Kim and Barnes 2005, Jaeheung et al. 2005, Weiss and Dahlstrom 2006, Schulwitz and Mortazawi 2006, Worms et al. 2006, Jaeheung et al. 2007, Worms et al. 2007).

Rotman lenses have been implemented using fiber optic cables. The optical couplers and delay lines are used to implement true-time-delay beam-forming. The delay lines are trimmed to achieve the appropriate amplitudes and phase shift for a signal driving a linear array antenna. A similar scheme has been described for RF direction finding applications, and a holographic Rotman lens using diffractive optic elements in free space has been demonstrated (Curtis 1995). This approach has been used to create a four beam, four element, photonic beamformer to drive a 2 to 4 GHz array (Sparks et al. 1998). This was expanded to an eight beam, sixteen element, photonic Rotman lens (Sparks et al. 1999, Sparks 2000, van Vliet 2002, Rotman et al. 2005).

4.5 Chapter Summary

This chapter has reviewed the advancements made in Rotman lens theory and design. It has presented the Rotman design equations, the effect each parameter has on lens

geometry, and the accepted method of evaluating geometrical errors. This is a basis for the contributions this thesis has made to geometrical optics analysis and optimisation of the Rotman lens. In the following chapter the Rotman equations are rewritten in a form suited to a feed network for a linear array and redefines the definition of aberrations to have greater relevance to the beam-forming ability of the lens.

While the Rotman equations are based on geometrical optics, electromagnetic models must be used to predict the behaviour of the lens. This is best carried out by treating each port as a two dimensional antenna element matched to a transmission line. Coupling between ports has been found using a number of electromagnetic simulation methods. However, there is little understanding of the precise mechanisms that limit lens performance. It is the answer to this question that is the largest contribution of this thesis, and is presented in the following chapter.